PROGRAMME
INFRASTRUCTURES MATERIELLES ET
LOGICIELLES POUR LA SOCIETE
NUMERIQUE – ED. 2011

Project Acronym	CORMORAN (ANR 11-INFR-010)
Document Title	D2.1 - On-Body Antennas Characterization & Exploitable Radiation Properties
Contractual Date of Delivery	M10 (31/10/2012)
Actual Date of Delivery	M13 (15/01/2013)
Editor	UR1
Authors	Meriem Mhedhbi, Stéphane Avrillon, Bernard Uguen, Melsuine Pigeon, Raffaele D’Errico, Pierre Pasquero
Participants	CEA, UR1
Related Task(s)	T2
Related Sub-Task(s)	T2.1
Security	Public
Nature	Technical Report
Version Number	1.0
Total Number of Pages	57

TABLE OF CONTENT

ABSTRACT

This document describes the work realized on the on-Body antennas characterization in the CORMORAN project. A first dedicated measurement campaign is described. Several series of measurements have been performed in order to feed the modeling task. The resulting model exploits a sparse and compact representation of the vector radiating function of UWB antennas. More specifically two different spherical harmonics decomposition schemes have been studied and implemented, namely the vector spherical harmonics and scalar harmonics decompositions. Several key intermediary steps made towards the elaboration of the final model are presented herein, including an in-depth analysis of the behavior of the spherical harmonics with respect to the antenna-cylinder distance. This model is going to become in turn an important building component of the overall CORMORAN simulator. Other series of measurements, which have been intended and designed for the purpose of studying the effect of the radiation pattern with respect to the antenna-phantom distance are also analyzed. A preliminary model is thus proposed to account for the variation of the coefficients' modulus only. The model related to the phase variation is however still hard to determine out of this early data analysis. A preliminary attempt to solve this problem by using a simple geometrical optics model is then also presented. Finally, as a complementing contribution to the previous work, the on-body behavior of a set of antennas, used for WBAN channel measurements in CORMORAN, has been analyzed through extensive electromagnetic simulations.

EXECUTIVE SUMMARY

This document presents preliminary studies and results on antenna modeling. It consists first in the description of a measurement campaign which has been performed in the near field chamber of IETR for the purpose of characterizing the effect of a human phantom on antennas' radiation patterns. Different series of measurements have been performed and carefully described. The collected database of various UWB antennas will be used later as a library of possible radiating elements and incorporated in the overall CORMORAN simulator (i.e. involved in deterministic location-dependent physical simulations). The proposed model, which will be used in this simulation chain for compactness reasons, will exploit sparse spherical harmonics decompositions. Two decompositions have indeed been implemented and described in the very document. An attempt to make a fair comparison between the two approaches is however still ongoing (but shall be reported in more details into the next deliverable regarding wide-sense radio channel characterization and modeling).

In order to take into account the radiation patterns of such antennas in the vicinity of the body, a simplified model based on a canonical shape has been imagined and a dedicated measurement series (series 2) has been performed. The careful analysis of this series 2 radiation patterns allows us to extract a simple model for the modulus of the scalar spherical harmonics. One remaining issue concerns the phase, which exhibits a non-random behavior that is hard to model. A pure statistical model would fail to preserve the directivity information, which is required for the foreseen application of the model into the final simulator. A new approach based on the geometrical optics has thus been recently figured out and currently investigated. The first general elements of this model are presented in the last section of this document.

1. INTRODUCTION

This report is related to the subtask 2.1 of the CORMORAN project. This subtask focuses on investigating and modeling the interaction of the antenna with the body, according to its orientation and proximity.

In the WBAN radiolocation and/or cooperative networking context it is not always enough to produce a statistical model to capture realistically the behavior of the radio received signal with on-body antennas. It is additionally required that this reproduced variability is correlated to the underlying human motion and physical contextual environment. Indeed the placement of a moving antenna on (or close to) a human body strongly affects its radiation properties and hence, it is no more rigorous to use a static free space description.

In this subtask, the characterization of body-worn antennas relies on a specific over-the-air (OTA) test-bed in anechoic chamber and a near-field antenna measurement chamber. The goal is to produce a dedicated measurement dataset and to build a good abstraction of antennas for the physical simulator developed in subtask ST2.4. Specific considerations on radiation properties will be drawn from the perspective of the localization application (e.g. in terms of coarse Angle Of Arrival -AOA- estimation, possible fusion with inertial units to compensate for antenna misalignments while interpreting Time Of Arrival -TOA- estimates, etc.). Assuming at least a coarse knowledge of the antenna orientation (e.g. through simple embedded inertial sensors in a real system), the characterized radiating properties of on-body antennas could also help to enhance further the cooperative WBAN communication and localization functionalities (e.g. through compensated directivity variations, spatial filtering, coarse AOA estimation…). The work plan and steps for this subtask are as follows:

- perform dedicated measurements in order to exhibit proper compact descriptions suitable for further WBAN channel simulations;
- extend the Vector Spherical Harmonics (VSH) description framework to WBAN contexts;
- study the VSH coefficients' behavior with various relevant positions on (or close to) the human body;
- propose a statistical model for moving WBAN antennas and time variations of VSH coefficients.

This document is structured as follows. In section 2, we describe the specific measurement campaigns carried out at UR1 premises in a near-field chamber based on a dielectric phantom, including aspects related to the measurement set-up and data pre-/post-processing. Then in section 3 we introduce theoretical concepts on the vector and scalar Spherical Harmonics (V/SSH) decomposition. Section 4 recall the first observations made out of the extracted measurement data, regarding particularly the evolution of the radiation pattern and SH coefficients of on-body antennas. Then we present the first model derived to account for the body effect on antennas. Finally, we provide complementary simulation results regarding on-body antennas used for WBAN (wide-sense) radio channel characterization.

2. MEASUREMENT CAMPAIGN DESCRIPTION

2.1. INTRODUCTION

A two-day antenna measurement campaign has been performed at the IETR using the near field measurement chamber at INSA, Rennes, France, April 12&13, 2012. The objective of the campaign was to collect data for characterizing of the variability of the radiation pattern of ultra wideband (UWB) antennas due to antenna structure and vicinity of the human body, in the measurement represented by the phantom of an arm.

The measurement campaign was planned and carried out by a team consisting of:

- Prof. Bernard Uguen (IETR, University Rennes 1, France)
- Associate Prof Stephane Avrillon (IETR, University Rennes 1, France)
- Assistant Prof. Mohamed Laaraiedh (IETR, University Rennes 1, France)
- PhD Student Meriem Mhedhbi (IETR, University Rennes 1, France)
- Associate Prof. Troels Pedersen (NavCom, Aalborg University, Denmark)

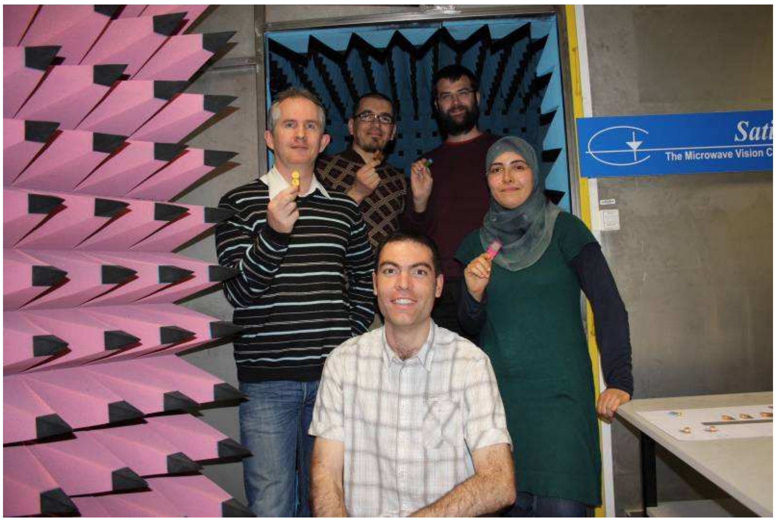

Figure 2-1 Measurement team after the completed measurement campaign

2.2. MEASUREMENT SETUP

The measurement campaign was carried out in the Satimo SG32 near-field antenna measurement chamber at INSA.

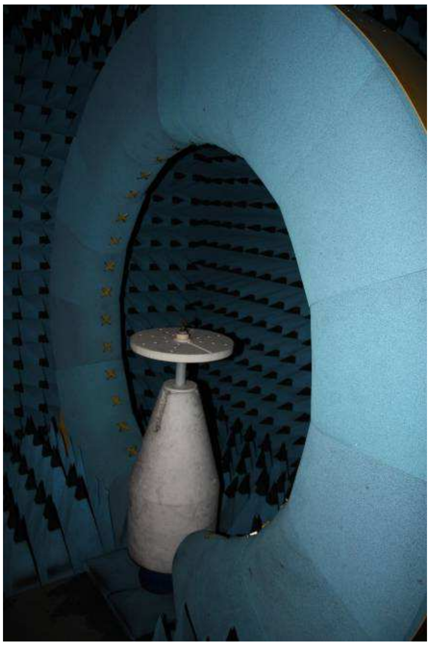

Figure 2-2 The measurement platform placed in the anechoic chamber on Satimo positioner. The cross-shaped probes are also visible in the SG32 measurement arch.

2.2.1 MEASUREMENT PLATFORM

The antennas and phantom were mounted on a platform custom build for the measurement campaign. See Figure 2-3. It is dedicated to have antenna measurements in presence of phantom in different directions and distances from this antenna. The platform was made of dielectric with $\varepsilon_r \approx 1$ such that the impact to the platform could be kept at a minimum. A distance scale on the bottom side of the platform was used to measure the position of the phantom in the groove. As can be seen in Figure 2-3, the holes in the platform were labelled for easy reference.

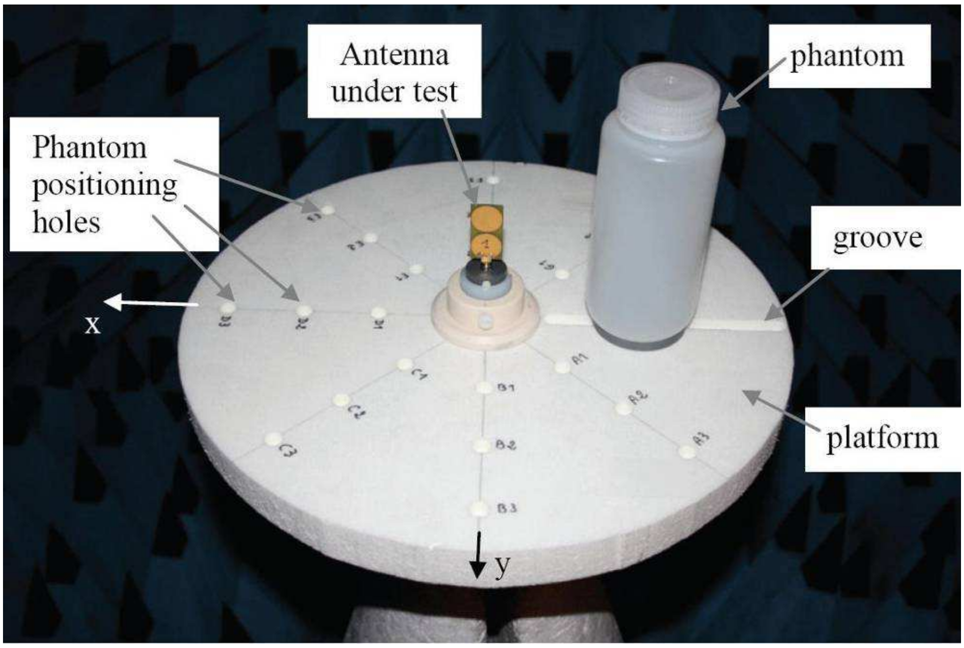

Figure 2-3 Measurement platform with coordinate system

2.2.2 SYSTEM FOR ANTENNA AND PHANTOM POSITIONING SYSTEM

A main cylinder stand is fixed with the Stargate positioner. A bottom washer and a top flange permit to fix the platform on the stand. A removable tube is inserted in the main cylindrical stand in order to fix the antenna.

- Main cylinder stand Material: Bottom part in Teflon, Main cylinder in PA6 Nylon. Function: to fix the platform with the StarGate positioner at a suitable height (middle of the Stargate) Figure 2-4
- Bottom washer Function: to fix the platform with the StarGate positioner at a suitable height (middle of the Stargate) Function: To stabilize the platform
- Platform Material: In Rohacell. Function: To place phantom at different positions around the antenna Figure 2-5
- Top flange Material: In white PVC. Function: To fix the platform Figure 2-6 **Erreur ! Source du renvoi introuvable.**
- Removable tube Material: In PVC. Function: To fix the antenna in the main cylinder Figure 2-6

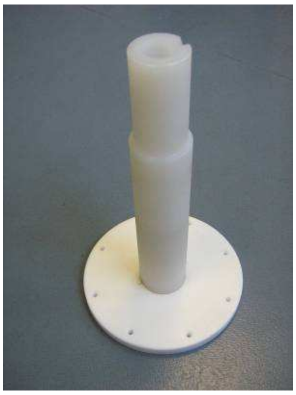

Figure 2-4 Main cylinder stand

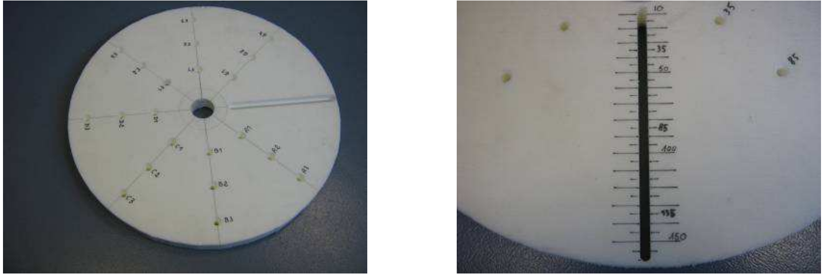

Figure 2-5 Photos of platform on two sides

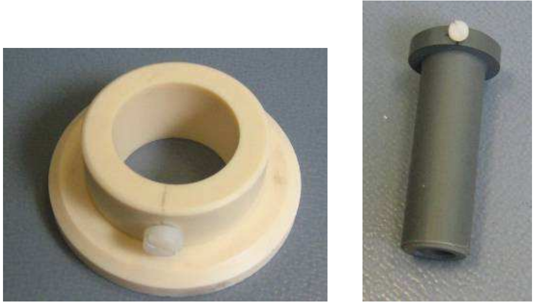

Figure 2-6 Photos of top flange (left) and removable tube (right)

- *Platform fixing system*

The platform is fixed on the main cylinder stand using the flange and a screw. The removable tube which is inserted into the main cylinder permits to fix the antenna connector using a small plastic screw. See Figure 2-7.

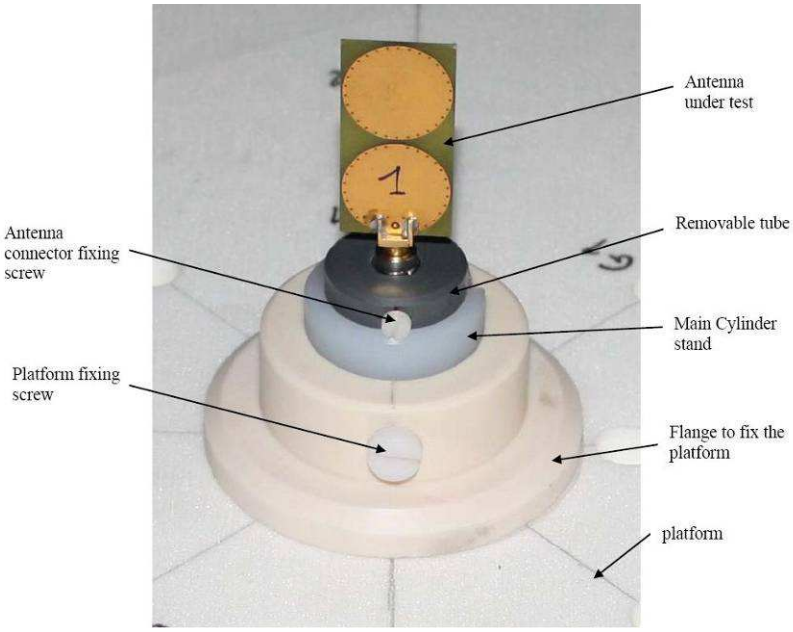

Figure 2-7 Detailed view of the platform and antenna fixing system.

- *Phantom positioning groove and holes*

The platform has two different phantom positioning capabilities:

- The groove graduated from 10mm to 160mm, which is the distance measured from the bottom washer. See Figure 2-8.
- 21 positioning holes named with letters indicating the angle (A=45°, B=90°, C=135°, D=180°, E =225°, F=270°, and G=315) with respect to the groove and with numbers indicating the distance from the bottom washer. See Figure 2-8.

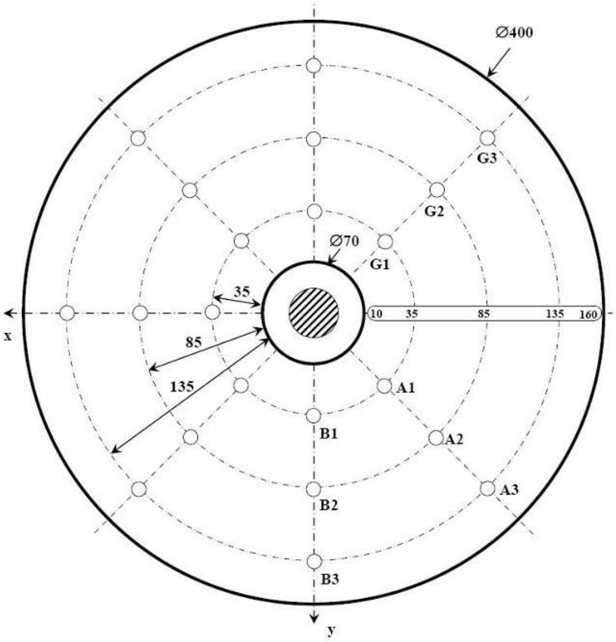

Figure 2-8 Detailed description of holes and groove positions.

2.2.3 PHANTOM

The custom built phantom (depicted in Figure 2-9 was a nearly cylindrical plastic bottle filled with MSL1800 phantom liquid. The size of the phantom was chosen to represent that of a human arm, while still being light enough for the platform to support it. The bottle was fitted with a screw in the bottom to allow for mounting on the platform groove or holes.

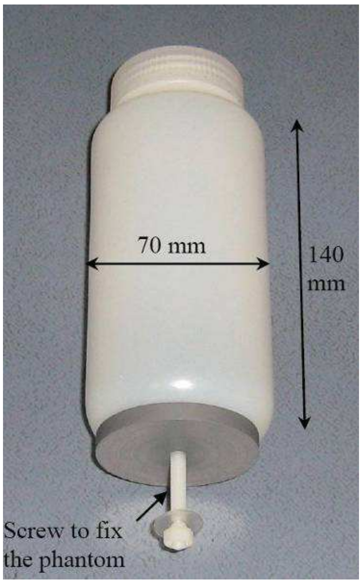

Figure 2-9 Phantom used in the measurement.

2.2.4 ANTENNAS

To allow for statistical description of the radiation pattern, we measured radiation patters of in total 17 UWB antennas. The antennas are listed in Table 2.1 and depicted in Figure 2-10. The antennas were photographed one by one next to a ruler for possible later use in publication. Also the S_{11} patterns were measured using a network analyzer. The antennas are chosen to have roughly similar characteristics, but to represent different kinds and make. Some antennas (Th1–Th4 and F1&F2) were of identical type.

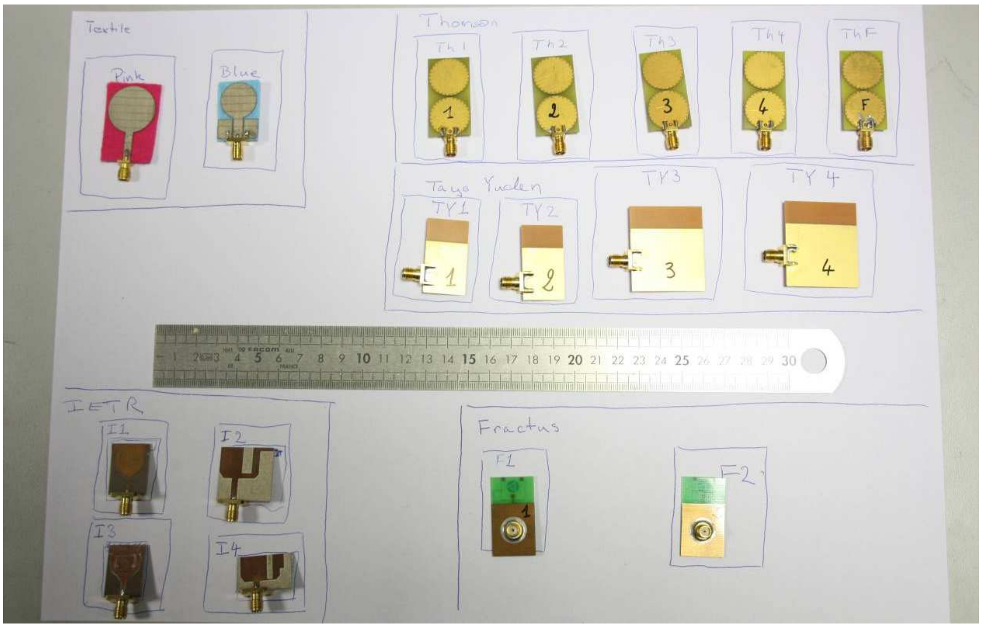

Figure 2-10 The 17 UWB antennas used in the measurement. To keep track of the antennas during measurement they were stored (when not in use) on a marked sheet of paper with the names, photo filename and drawings.

Label	Manufacturer	Photo	Comment
Th1	Thomson	IMG_2856.JPG	Ref [2]
Th2	Thomson	IMG_2857.JPG	Ref [2]
Th3	Thomson	IMG_2858.JPG	Ref [2]
Th4	Thomson	IMG_2859.JPG	Ref [2]
ThF	Thomson	IMG_2860.JPG	Ref [2] Notch filtering antenna
TY1	Tayo Yuden	IMG_2861.JPG	Ref [3]
TY2	Tayo Yuden	IMG_2862.JPG	Ref [3]
TY3	Tayo Yuden	IMG_2863.JPG	Ref [3]
TY4	Tayo Yuden	IMG_2864.JPG	Ref [3]
F1	Fractus	IMG_2866.JPG	Ref [4]
F2	Fractus	IMG_2868.JPG	Ref [4]
TexPink	IETR	IMG_2869.JPG	Textile Antenna, Nacer Chahat, Unpublished
TexBlue	IETR	IMG_2870.JPG	Textile Antenna, Nacer Chahat, Unpublished
I1	IETR	IMG_2871.JPG	Monopole
I2	IETR	IMG_2872.JPG	Ref [5]
I3	IETR	IMG_2873.JPG	As I1, but with a frequency notch
I4	IETR	IMG_2874.JPG	Derived from I2, Unpublished

Table 2.1 Antennas used in the experiments

2.3. MEASUREMENT SERIES

The complete measurement campaign consists of measurement series. Each series consists of number of runs. A measurement run is defined as one antenna measurement resulting in one data file.

A photo was taken of the platform and antenna was taken prior to each measurement run. Care was taken to have the same perspective for all photos such that The photos where taken using a handheld camera, but we strived at obtaining the same view every time to allow us to use the photos as a kind of "stop-motion" movie of the phantom settings for S2 and S3.

Naming convention: Run X of Series Y is named SXRY, e.g. S1R5 is Series 1 Run 5.

2.3.1 MEASUREMENT SERIES S1

The primary focus of S1 is to collect measurements data of the antennas listed in Table 2.1. The antennas were one by one placed in the measurement platform without the phantom.

S1R1–S1R17: Measurements of antennas listed in Table 2.1.

2.3.2 MEASUREMENT SERIES S2

The purpose of this measurement series is to measure how the antenna response varies in the presence of the phantom at various antenna-phantom distances. Antenna Th1 was used for all runs of series S2. The phantom was placed in the groove.

S2R1: Re-calibration without phantom (Same setting and antenna as in S1R1)

S2R2–S2R21: Measurement with phantom at different radial distances using the groove. We start by minimum distance and increase the distance in steps of 5 mm.

2.3.3 MEASUREMENT SERIES S3

The purpose of S3 is to measure how the antenna response varies with phantom-antenna angle and distance. Antenna Th1 was used for all runs of series S3. The phantom-antenna angle and distance varies using the wholes, and at three positions in the grove.

S3R1: Re-calibration without phantom (Same setting and antenna as in S1R1)

S3R2–S3R4: Phantom placed in the grove at distances matching the distances of the holes.

S3R5-S3R25: The phantom is placed in the holes.

2.3.4 MEASUREMENT SERIES S4

The measurement series S4 is an auxiliary measurement series containing some measurements with the common purpose to ensure the integrity of the data after post-processing and to evaluate the repetition error or he measurement technique.

S4R1–S4R2: Metal screen fixed on phantom. This gives a strongly directive pattern with main lobe opposite to the screen, which may be used to ensure that we can interpret the angles recorded by Satimo unambiguously and transform these into the defined coordinate system on the platform. S4R1 with the phantom placed in the groove at distance 35 mm, and S4R2 with the phantom in position F1. See Figure 2-11.

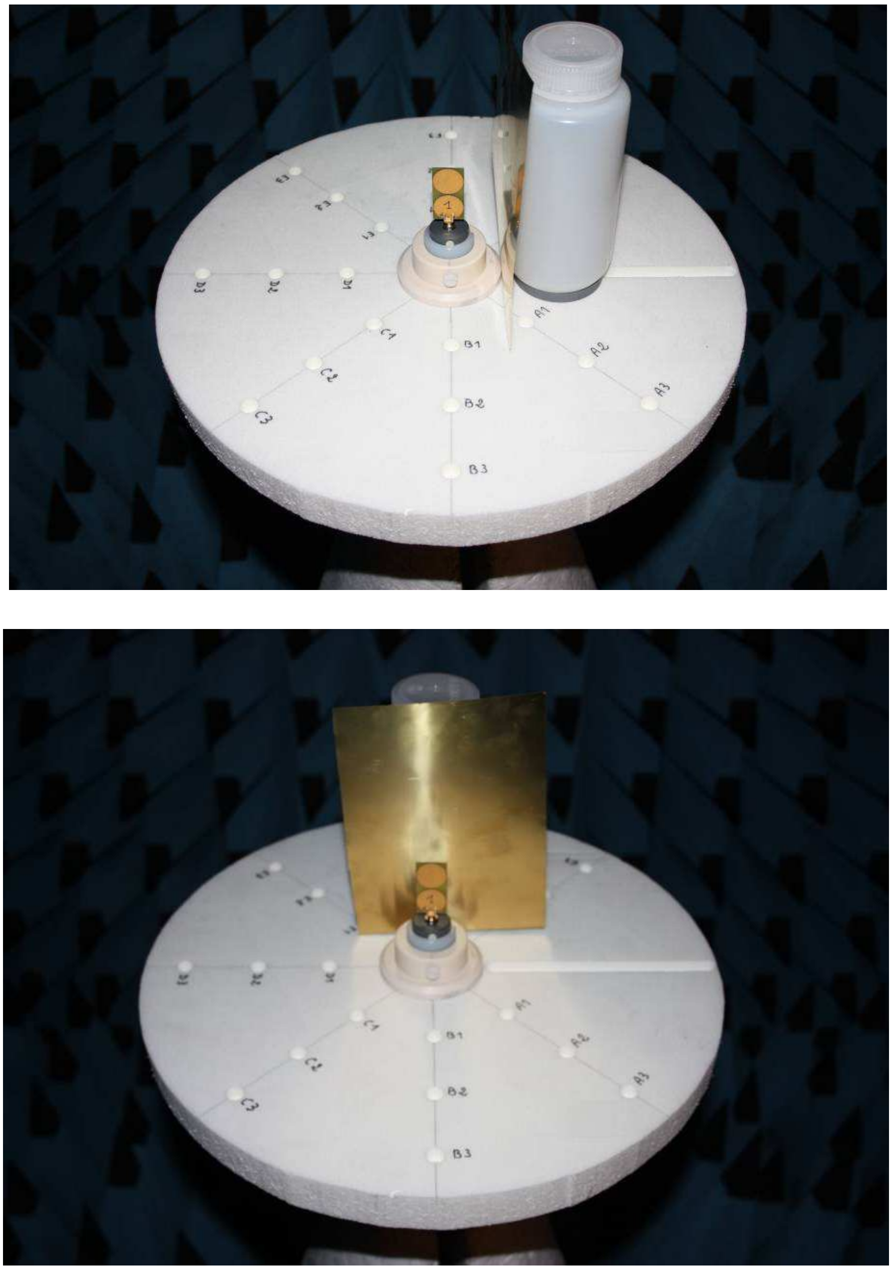

Figure 2-11 Setup for S4R1 (left) and S4R2 (right).

S4R3–S4R6: Changing the antenna orientation with respect to the platform. Notice that S4R3 is with the same orientation as used in all measurement runs, except S4R4, S4R5, and S4R6. Thus S4R3 may also be used to compare repeatability of the calibration measurement for antenna Th1.

S4R7–S4R8: The antenna was unmounted, then mounted in the platform again in the standard orientation and then measured without the phantom. These two runs will, together with the S1R1, S2R1, S3R1 and S4R3 allow for evaluation of the repeatability of the measurement procedure.

S4R9: The measurement was performed with and empty phantom, i.e., with the plastic container alone without phantom liquid. This will allow for the evaluation of the impact of the plastic container itself.

2.4. MEASUREMENT LOG

During the measurement campaign, the setup and filenames of photos and measurement data where recorded in an excel file which served as a measurement log. In addition, during the measurements, handwritten notes documented the procedure.

2.4.1 MEASUREMENT DAY 1: APRIL 12

The S_{11} was measured for the 17 antennas using a vector network analyzer prior to the measurements in the near-field chamber. The measurement equipment was set up and performed several test runs. Some startup problems were sorted out with the help of Jerome Sol.

Measurements S1 started after setup and instruction at 16:00h and ended at approximately 18:00 (approximately). The duration of each measurement run was 6 to 7 min. Start time of each run was entered in the measurement log. Photos of the setup in the platform were taken before each measurement run and the filename of the photo was entered in the log. Measurement data was exported in ASCII txt format in a .trx file for easy access. The filenames of photos and antenna data files are all entered in the measurement log.

Measurement apparatus is left ON overnight to avoid startup difficulties on Day 2.

2.4.2 MEASUREMENT DAY 2: APRIL 13

Overnight, Bernard checked some of the data during the evening to see if there should be any problems with the data. He detected some problem with the definition of the coordinate system used by the Satimo equipment. Apparently the Satimo chamber uses a left-handed coordinate system with strange ranges for the co-elevation and azimuth angles. To eliminate any ambiguity in the use of the data it was decided to perform the runs S4R1 and S4R2, where a metal screen ensured an antenna radiation pattern with a strong main-lobe in a controlled direction. The measurements continued using the same format as we started to keep data consistent. The data was transformed into a natural right-handed coordinate system.

The measurement data was transferred from the measurement computer. Also, the probe-corrected nearfield data was exported and stored in ASCII format. This data may be later transformed using a custom algorithm to perform the near-field to far-field transformation.

2.4.3 PRINTOUT OF LOGFILE

Meas. Series	Meas. run	Ant	Phant	Phant. pos.	Phant. dist.	Photo file	Data file	Date	Start time	Notes
1	1	Th1	No			100-2839	S1R1	04/12/12	15:55	Mohamed at the log
1	2	Th2	No			100-2840	S1R2	04/12/12	16:03	
1	3	Th3	No			100-2841	S1R3	04/12/12	16:09	
1	4	Th4	No			100-2842	S1R4	04/12/12	16:18	

1	5	ThF	No			100-2843	S1R5	04/12/12	16:24	
1	6	TY1	No			100-2844	S1R6	04/12/12	16:30	
1	7	TY2	No			100-2845	S1R7	04/12/12	16:35	post processing re-done due to export error
1	8	TY3	No			100-2846	S1R8	04/12/12	16:41	
1	9	TY4	No			100-2847	S1R9	04/12/12	16:52	
1	10	F1	No			100-2848	S1R10	04/12/12	16:57	
1	11	F2	No			100-2849	S1R11	04/12/12	17:04	
1	12	TexPink	No			100-2850	S1R12	04/12/12	17:11	
1	13	TexBlue	No			100-2851	S1R13	04/12/12	17:17	
1	14	I1	No			100-2852	S1R14	04/12/12	17:24	
1	15	I2	No			100-2853	S1R15	04/12/12	17:30	
1	16	I3	No			100-2854	S1R16	04/12/12	17:36	
1	17	I4	No			100-2855	S1R17	04/12/12	17:42	
4	1	Th1	See note	groove	40	100-2875	S4R1	04/13/12	09:27	metallic screen attached to empty phantom
4	2	Th1	See note	F1		100-2876	S4R2	04/13/12	09:37	metallic screen attached to empty phantom
2	1	Th1	No			100-2877	S2R1	04/13/12	09:49	reference measurement run
2	2	Th1	Yes	groove	30	100-2878	S2R2	04/13/12	09:59	
2	3	Th1	Yes	groove	35	100-2879	S2R3	04/13/12	10:08	
2	4	Th1	Yes	groove	40	100-2880	S2R4	04/13/12	10:14	break after this run
2	5	Th1	Yes	groove	45	100-2881	S2R5	04/13/12	10:48	
2	6	Th1	Yes	groove	50	100-2882	S2R6	04/13/12	10:55	
2	7	Th1	Yes	groove	55	100-2883	S2R7	04/13/12	11:03	
2	8	Th1	Yes	groove	60	100-2884	S2R8	04/13/12	11:08	
2	9	Th1	Yes	groove	65	100-2885	S2R9	04/13/12	11:16	
2	10	Th1	Yes	groove	70	100-2886	S2R10	04/13/12	11:22	
2	11	Th1	Yes	groove	75	100-2887	S2R11	04/13/12	11:28	
2	12	Th1	Yes	groove	80	100-2888	S2R12	04/13/12	11:34	
2	13	Th1	Yes	groove	85	100-2889	S2R13	04/13/12	11:40	
2	14	Th1	Yes	groove	90	100-2890	S2R14	04/13/12	11:46	
2	15	Th1	Yes	groove	95	100-2891	S2R15	04/13/12	12:59	Reboot of Satimo needed only Bernard, Troels and Stephane present, Troels at the log
2	16	Th1	Yes	groove	100	100-2892	S2R16	04/13/12	13:05	Only Bernard, Troels and Stephane present
2	17	Th1	Yes	groove	105	100-2893	S2R17	04/13/12	13:12	Only Bernard, Troels and Stephane present
2	18	Th1	Yes	groove	110	100-2894	S2R18	04/13/12	13:19	Only Bernard, Troels and Stephane present
2	19	Th1	Yes	groove	115	100-2895	S2R19	04/13/12	13:25	Only Bernard, Troels and Stephane present
2	20	Th1	Yes	groove	120	100-2896	S2R20	04/13/12	13:31	Meriem joined again
2	21	Th1	Yes	groove	125	100-2897	S2R21	04/13/12	13:27	Mohamed joined again
2	22	Th1	Yes	groove	130	100-2898	S2R22	04/13/12	13:44	
2	23	Th1	Yes	groove	135	100-2899	S2R23	04/13/12	13:51	
3	1	Th1	No			100-2900	S3R1	04/13/12	14:23	Mohamed at the log
3	2	Th1	Yes	groove	35	100-2901	S3R2	04/13/12	14:29	
3	3	Th1	Yes	groove	85	100-2902	S3R3	04/13/12	14:36	
3	4	Th1	Yes	groove	135	100-2903	S3R4	04/13/12	14:42	

3	5	Th1	Yes	A1		100-2904	S3R5	04/13/12	14:48	
3	6	Th1	Yes	A2		100-2905	S3R6	04/13/12	14:54	
3	7	Th1	Yes	A3		100-2906	S3R7	04/13/12	15:00	
3	8	Th1	Yes	B1		100-2907	S3R8	04/13/12	15:07	
3	9	Th1	Yes	B2		100-2908	S3R9	04/13/12	15:13	
3	10	Th1	Yes	B3		100-2909	S3R10	04/13/12	15:19	
3	11	Th1	Yes	C1		100-2910	S3R11	04/13/12	15:26	
3	12	Th1	Yes	C2		100-2911	S3R12	04/13/12	15:32	
3	13	Th1	Yes	C3		100-2912	S3R13	04/13/12	15:38	
3	14	Th1	Yes	D1		100-2913	S3R14	04/13/12	15:44	
3	15	Th1	Yes	D2		100-2914	S3R15	04/13/12	15:50	
3	16	Th1	Yes	D3		100-2915	S3R16	04/13/12	15:56	
3	17	Th1	Yes	E1		100-2916	S3R17	04/13/12	16:03	
3	18	Th1	Yes	E2		100-2917	S3R18	04/13/12	16:10	
3	19	Th1	Yes	E3		100-2918	S3R19	04/13/12	16:16	
3	20	Th1	Yes	F1		100-2919	S3R20	04/13/12	16:23	
3	21	Th1	Yes	F2		100-2920	S3R21	04/13/12	16:29	
3	22	Th1	Yes	F3		100-2921	S3R22	04/13/12	16:36	
3	23	Th1	Yes	G1		100-2922	S3R23	04/13/12	17:01	
3	24	Th1	Yes	G2		100-2923	S3R24	04/13/12	17:07	
3	25	Th1	Yes	G3		100-2925	S3R25	04/13/12	17:14	unfocused photo (100-2924)
4	3	Th1	No			100-2926	S4R3	04/13/12	17:27	Ant. Orient. B
4	4	Th1	No			100-2927	S4R4	04/13/12	17:33	Ant. Orient. D, antenna disconnected then connected
4	5	Th1	No			100-2928	S4R5	04/13/12	17:40	Ant. Orient. F, antenna disconnected then connected
4	6	Th1	No			100-2929	S4R6	04/13/12	17:47	Ant. Orient. Groove, antenna disconnected then connected
4	7	Th1	No			100-2930	S4R7	04/13/12	17:54	Another reference meas. Ant. Orient. B, antenna disconnected then connected
4	8	Th1	Yes	groove	35	100-2931	S4R8	04/13/12	18:00	Empty Phantom
										Finished at 18:10

2.5. POST-PROCESSING AND ORGANIZATION OF THE MEASUREMENTS

The collected data is post-processed to transform the coordinate system into a standard right-handed coordinate system with co-elevation $0 \leq \theta \leq \pi$ and azimuth $0 \leq \phi \leq 2\pi$. The data which comes out the Near Field to far field transformation are expressed in a coordinate system which is strongly related to the near field chamber. The data stored in the Matlab files have been processed to be expressed in a natural spherical coordinate system.

The transformation from chamber coordinate system (1) to the natural spherical coordinate system (2) (materialized in the near field in Figure 2-12 can be expressed as follow:

$$\theta_2 = |\theta_1|$$

$$\phi_2 = \phi_1 + (1 - \mathrm{sign}(\theta_1))\,\pi/2$$

The effect of this peculiar angular transformation for a given frequency index is illustrated in Figure 2-13.

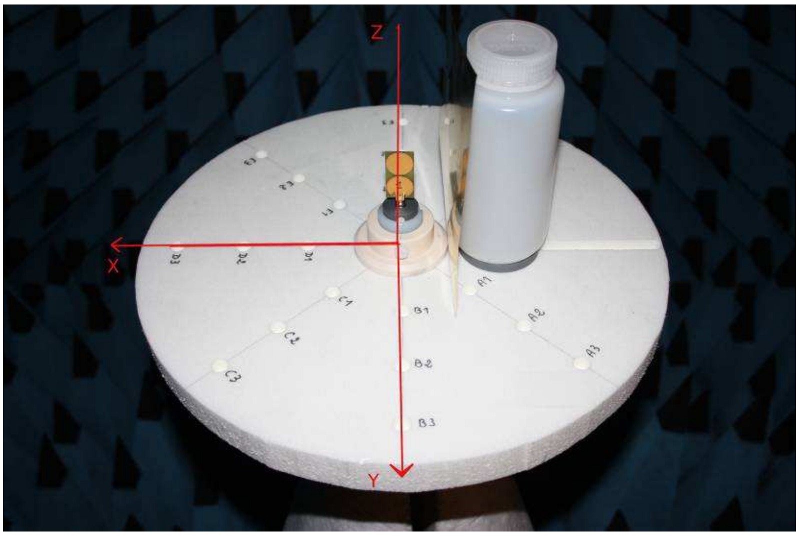

Figure 2-12 Natural coordinate system (2) represented in the Near Field Chamber - Photo Serie 4 Run 1

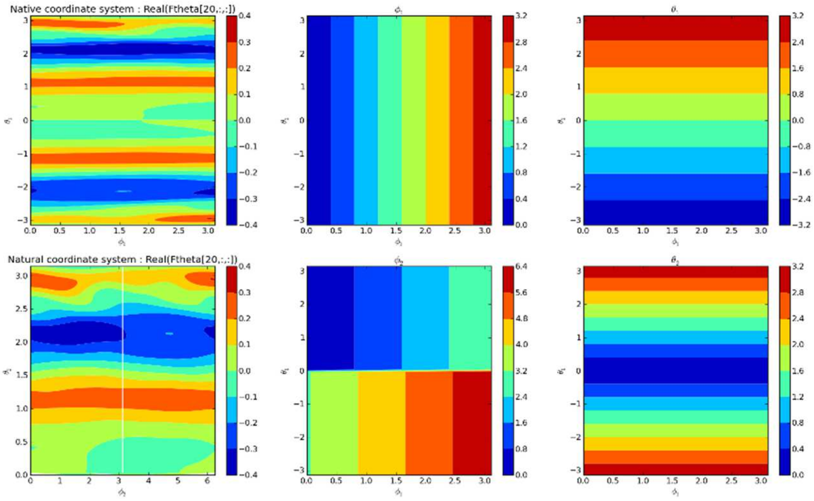

Figure 2-13 Effect of the coordinate system transformation, file S1R1.trx - frequency index 20

The data are gathered in the following directories:

- **NFTRX**: In this directory we have the ``trx`` files of the near field. These files provides a header which define the column representing the second part of the file namely, the frequency band and the sampling frequency, theta and phi ranges and the field component. This is the calibrated measures on each probe of the Stargate arch. This information is then post-processed using the Near Field to Far Field transform in order to get an ascii ``trx`` file containing the whole radiation information in the far field of the antenna. This information could be exploited later for validation of customized Near field to Far Field transform.

- **FFTRX**: this directory includes the ``trx`` files of the far field.
- **Matfile**: in this directory are gathered Matlab files of the different measurements series and runs. Each Matlab file is created from a corresponding python dictionary structure giving all the information about measurement series and runs :
  - Circumstance: Serie and Run numbers, date and Startime of the run
  - Antenna field data : AntennaName, phi, theta, Ftheta, Fphi and
  - frequency range
  - Related files: Photofile and Datafile
  - Observation: some Notes are included and the presence or absence of the Phantom is mentioned
- **S11**: In this directory are included S11 parameters of the 17 antennas used during the measurement campaign.
- **Documentation**: This report and various documents related to the near field chamber.
- **PhotosVideos**: The set of photos and videos related to this measurement campaign.

A specific Python script (parsedata.py) has been developed to transform far field .trx into Matlab Files.

2.6. KNOWN ERROR SOURCES

We estimate the displacement of the phantom in the groove is accurate to ±2mm.
We estimate that the phantom positions in the wholes, is accurate to ±1mm.
The SMA connectors of the antennas were tightened manually without control of the torque. However, the connector repeatability can be checked by runs S1R1, S2R1, S3R1, S4R3, S4R7, and S4R8.
The reference plane of the far field plane is delayed. A proper application of an electrical delay can be applied to compensate this effect which can be observe in and estimated from the data set.

3. SPHERICAL HARMONICS DECOMPOSITION

3.1. INTRODUCTION

There exist two kind of approach for decomposition of a vector field on a spherical harmonics basis. Either the vector field is decomposed on vector basis and it is referred as a vector spherical harmonics (VSH) decomposition, either each 3D component of the field is projected on a scalar basis and its is refereed as scalar spherical harmonics (SSH).
The spherical harmonics are a frequency space basis for representing functions defined over the sphere, just like the Fourier transform tool in one dimensional space. The spherical harmonics have been already used in several fields such as computer graphics, computation of atomic electron configurations…

Spherical harmonics are, also, useful in antenna field. In fact, it is an optimal tool to represent, compactly, the antenna radiation pattern using few parameters.

Traditionally, the representation of antenna pattern has been done using vector spherical harmonics with scalar coefficient. But, recent work [Rohala2009] investigates the use of scalar spherical harmonics with vector coefficients in order to represent the antenna radiation pattern. In this part, this method is adopted, and we start by explaining the mathematical formalism behind this approach.

In order to have realistic and accurate results from a propagation channel simulator, it imports to take into account the transmitting and receiving full vector antenna radiation patterns. Recent works have revealed the great interest of having such sparse representation. In this context, spherical harmonics comes up. This kind of representation is of interest at both fundamental [Roblin2008] and practical levels [Burghelea2009], [Burghela2012], [Schmitz2102]. It becomes utmost important in case of UWB antennas which full representation is intrinsically cumbersome [Wiesbeck2007], [Roblin2008]. A measured antenna represents an extremely large amount of data which is expensive and difficult to manage especially in ray tracing simulator. Therefore, a full data compression is crucial. Moreover, the knowledge of the antenna radiation pattern is required only for a reduced number of directions. The spherical harmonics decomposition allows an efficient angular reconstruction. This aspect is one of the great advantages of the approach.

Until now, in order to model the antenna radiation pattern using the spherical harmonics, two approaches were proposed. The first one is a Vector Spherical Harmonics (VSH) decomposition [Roblin2008], [Burghelea2009]. This method consists in projecting the antenna pattern on a vector spherical harmonics basis. The vector expansion is fully described in [Swarztrauber1993]. A recent work [Rohola2009] investigates the second approach with consist in the use of scalar spherical harmonics basis with vector coefficients in order to represent the antenna radiation pattern.

3.2. VECTOR SPHERICAL HARMONICS

3.2.1 THEORETICAL FORMULATION

Vector spherical harmonics eexpansion is an efficient solution for modeling antenna vector functions [Burghela2012], providing easy and efficient data access and good compression ratios. VSH expansion establishes a one-to-one correspondence between antenna vector function $\boldsymbol{F}(f,\theta,\phi)$ and a set of complex coefficients ($br_k(f)$, $bi_k(f)$, $cr_k(f)$, $ci_k(f)$) . Once the VSH coefficients are computed, they allow to quickly reconstruct $\boldsymbol{F}_{ak}(fk,\theta k,\phi k)$.

The VSH synthesis relations can be expressed in matrix form as follows

$$\begin{cases} \boldsymbol{F}_\theta = \ \ \boldsymbol{Br}\cdot\overline{\boldsymbol{Vr}} - \boldsymbol{Bi}\cdot\overline{\mathbf{Vi}} + \boldsymbol{Ci}\cdot\overline{\boldsymbol{Wr}} + \boldsymbol{Cr}\cdot\overline{\boldsymbol{Wi}} \\ \boldsymbol{F}_\phi = -\boldsymbol{Cr}\cdot\overline{\boldsymbol{Vr}} + \boldsymbol{Ci}\cdot\overline{\mathbf{Vi}} + \boldsymbol{Bi}\cdot\overline{\boldsymbol{Wr}} + \boldsymbol{Br}\cdot\overline{\boldsymbol{Wi}} \end{cases}$$

where:

- F^{θ}, F^{ϕ} are two ($N_f \times N_r$) matrices associated with antenna vector functions on both polarization states, with N_f, N_r the number of frequency points and the number of rays.

- $\mathbf{B}_r$, $\mathbf{B}_i$, $\mathbf{C}_r$, $\mathbf{C}_i$ are four ($N_f \times N_k$) matrices associated with VSH coefficients. These coefficients are calculated for each frequency point of the antenna radiation pattern. They are uniquely indexed by an integer $k \in \{0, \ldots, N_k - 1\}$. This indexation scheme is an ad-hoc unambiguous, one-dimensional labeling of both longitude and colatitude. The number N_k of VSH coefficients depends on antenna type and dimensions with respect to the smallest wavelength and on radiation pattern frequency step
- $\bar{V}_r, \bar{W}_r, \bar{V}_i, \bar{W}_i$ are four ($N_k \times N_r$) matrices associated with the real and imaginary parts of VSH basis functions.
- The VSH synthesis of an antenna vector function can be limited to the essential coefficients in order to reduce data for storage, because many VSH coefficient values O_k are negligible over the entire considered frequency band for different indices k.
- The VSH synthesis of an antenna vector function can be limited to the essential coefficients in order to reduce data for storage, because many VSH coefficient values O_k are negligible over the entire considered frequency band for different indices k.

3.2.2 EXAMPLE OF DECOMPOSITION

At the beginning of the project, we have experienced some difficulties in implementing the vector spherical harmonics decomposition on the measured data due to an error in the computational implementation of the algorithm. This problem is now fixed and this approach is fully operational. Meanwhile, this problem has drive us to investigate for the alternative SSH approach presented in section 3.3

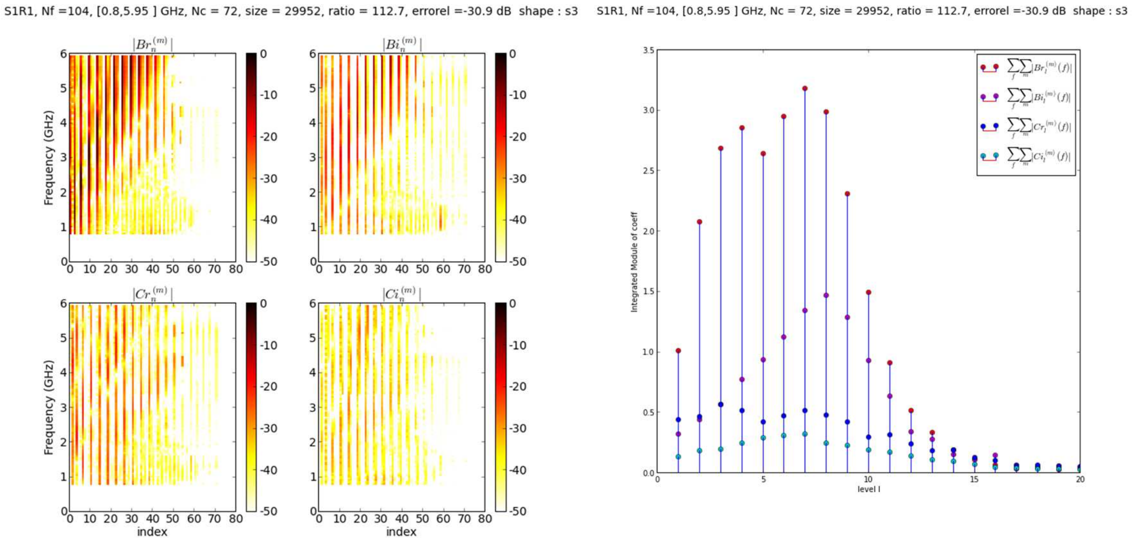

Figure 3-1 S1R1 thresholded VSH coefficients (left) w.r.t frequency and folded index and (right) integrated over m and frequency w.r.t level l

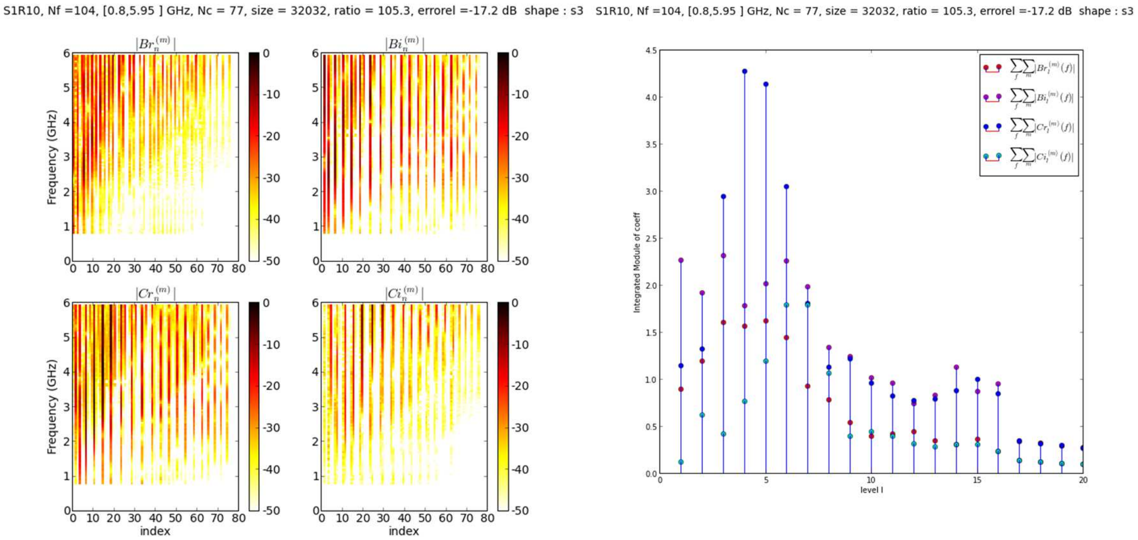

Figure 3-2 S1R10 thresholded VSH coefficients (left) w.r.t frequency and folded index and (right) integrated over m and frequency w.r.t level l

Figure 3-1 and Figure 3-2 represent the 4 complex vector spherical coefficients obtained for the reference Thomson 1 antenna. The Series 1, Run 1 corresponding to file S1R1.mat is here represented. The compressed file is smaller, by a factor of 112.7, than the original file. The overall relative error, which is defined as the energy of the difference between original and compressed, normalized with respect to the energy of the original file is equal to -30.9 dB. The reconstruction difference is unnoticeable (see Figure 3-3). Those figures have been produced for all the files of the measurement campaign database (Original data stored as mat files and the compressed version of vsh coefficient stored as new defined vsh3 files) and uploaded on the web server of the project.

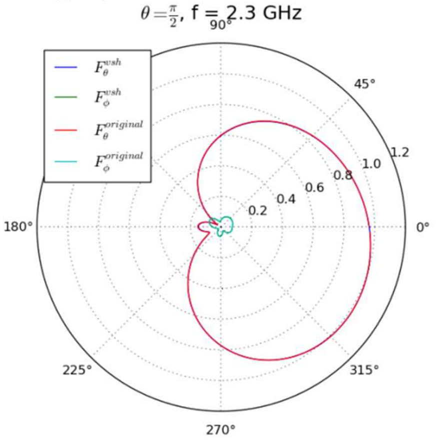

Figure 3-3: Azimuth pattern from both S2R3.mat and S2R3.vsh3

3.3. SCALAR SPHERICAL HARMONICS

3.3.1 SPHERICAL HARMONICS

- *Definition*

A harmonic is a function that satisfies Laplace's equation:

$$\nabla^2 f = 0$$

As their name suggests, the spherical harmonics are an infinite set of harmonic functions defined over the sphere. They arise from solving the angular portion of Laplace's equation in spherical coordinates using separation of variables.

The scalar spherical harmonics are defined by:

$$Y_l^m(\theta,\phi) = \sqrt{\frac{(2l+1)(l-m)!}{4\pi(l+m)!}} P_l^m(\cos\theta) e^{im\phi}$$

Where, P_l^m are the associated Legendre polynomials.

The basis' functions are indexed according two integer constants, the level, l, and the mode, m, which satisfies the constraint that l is an integer and $-l \le m \le l$, thus there are $2l + 1$ basis functions of level l.

The level l determines the spatial frequency of the basis' functions over the sphere, in fact, a basis function vanishes on (l-m) lines of latitude and $2m$ lines of longitude.

- *Projection*

The spherical harmonics defines a complete basis over the sphere, thus any spherical function F can be expanded as follows:

$$F(\Omega) = \sum_{l=0}^{\infty} \sum_{m=-l}^{l} f_l^m Y_l^m(\Omega)$$

where the coefficients f_l^m can be computed by either projecting F on each basis function Y_l^m or a linear least square method.

3.3.2 CALCULATION OF THE SPHERICAL HARMONICS COEFFICIENTS

In this section, we are using the same formalism in [Rahola2009]. The spherical harmonic of level l and mode m is given by:

$$Y_l^m(\theta,\phi) = K_{lm} P_l^m(\cos\theta) e^{jm\phi}$$

The far-field of the antenna radiation pattern can be expressed in terms of linear combination of spherical harmonics with vector coefficient $\mathbf{a}_{lm}$:

$$\mathbf{E}(\mathbf{r}) = \sum_{l=0}^{\infty} \sum_{m=-l}^{l} \mathbf{a}_{lm} \cdot Y_l^m(\mathbf{r})$$

Where $\mathbf{r}=\mathbf{r}(\theta,\phi)=(\sin\theta\cos\phi, \sin\theta\sin\phi, \cos\phi)$ is the unit vector to the direction represented by (θ,ϕ).

As it has been mentioned, traditionally, the vector spherical harmonics have been used to represent the antenna radiation pattern with scalar coefficients:

$$\mathbf{E}(\mathbf{r}) = \sum_{l=0}^{\infty} \sum_{m=-l}^{l} (a_{lm}\mathbf{V}_{lm}(\mathbf{r}) + b_{lm}\mathbf{W}_{lm}(\mathbf{r}))$$

In the far-field, the expression of the electric field takes the following form:

$$E_\theta = \sum_{l=0}^{\infty} \sum_{m=-l}^{l} (a'_{lm}(-jm)\frac{Y_l^m(\mathbf{r})}{\sin\theta} + b'_{lm}\frac{dY_l^m(\mathbf{r})}{d\theta})$$

$$E_\phi = \sum_{l=0}^{\infty} \sum_{m=-l}^{l} (a'_{lm}\frac{dY_l^m(\mathbf{r})}{d\theta} + b'_{lm}(-jm)\frac{Y_l^m(\mathbf{r})}{\sin\theta})$$

Following this representation it appears that both E_θ and E_θ are not continuous functions over the sphere since, their values change on the poles for different azimuths. To avoid this singularity, we resort to express the electric far-field in the scalar spherical basis using vector coefficient expressed in Cartesian coordinates system. Therefore we start by converting data from spherical coordinates to Cartesian coordinates.

$$\mathbf{e_c}(\mathbf{r_k}) = \mathbf{T}(\mathbf{r_k})\mathbf{e_s}(\mathbf{r_k})$$

Where $\mathbf{e_s}(\mathbf{r_k}) = [E_{\phi(\mathbf{r_k})}, E_{\theta(\mathbf{r_k})}]^T$ is the expression of the electric field in the spherical coordinates at K points on the sphere and $\mathbf{T}(\mathbf{r})$ is the transformation matrix:

$$\mathbf{T}(\mathbf{r}) = \begin{bmatrix} \sin\phi & \cos\phi & 0 \\ \cos\theta\cos\phi & \cos\theta\sin\phi & -\sin\theta \end{bmatrix}^T$$

For a given electric field, the coefficients $\mathbf{a}_{lm}$ can be obtained using an integration method, exploiting the orthonormality property of the scalar harmonic basis. Otherwise, we can use a least square method to solve the linear equations system given by equation [eq_Er]. During this work we opt for the second method which will be described in the rest of this section.

The antenna far-field $\mathbf{E_c}$ in Cartesian coordinates system can be related to the spherical harmonics matrix **Y** through the equation:

$$\mathbf{E_c} = \mathbf{A}\,\mathbf{Y} \qquad \text{(eq\_Ec)}$$

where **A** is the spherical harmonics coefficient matrix.

- Far-field matrix

$\mathbf{E_c}$ is the electric far-field in Cartesian coordinates at all K measurement points is obtained by converting from spherical to Cartesian coordinates the measured data and given by:

$$\mathbf{E_c} = [\mathbf{E_c}(r_1), \ldots, \mathbf{E_c}(r_K)]$$

- Spherical harmonics matrix

The spherical harmonics matrix **Y** at all K measurement points is given by the following equation:

$$\mathbf{Y}=[\mathbf{y}^T(r_1), \ldots, \mathbf{y}^T(r_K)]$$

where for a given measurement point the set of scalar spherical harmonics can be written as a vector:

$$y(r_k) = [y_0(r_k), y_1(r_k), \ldots, y_L(r_k), y_{-L}(r_k), \ldots, y_{-1}(r_K)]$$

where L is the maximum spherical harmonics level ($l = 0, \ldots, L$) and $y_m(r)$ is the set of harmonics at the mode m is given by:

$$\mathbf{y_m}(\mathbf{r}) = \left[Y_{|m|}^{m}(\mathbf{r}),\;\; Y_{|m|+1}^{m}(\mathbf{r}),\;\; \cdots,\;\; Y_{L}^{m}(\mathbf{r})\right]$$

- Spherical harmonics coefficient matrix

Regarding the matrix **A** it represents the coefficient matrix and defined as follows:

$$\mathbf{A} = [a_x, a_y, a_z]$$

The equation eq_Ec is relating $\mathbf{E_c}$, **Y** and **A** only in noise-free measurements conditions, therefore in typical noisy measurements, the field is written as follows:

$$\mathbf{E_c} = \mathbf{A}\,\mathbf{Y} + \mathbf{N}$$

where **N** is the measurement noise.

The coefficient matrix **A** is obtained by a least square estimation:

$$\hat{\mathbf{A}} = \arg\min_{\mathbf{A}} ||\mathbf{E}_c - \mathbf{A}\mathbf{Y}||_F^2$$

Where $||\cdot||_F$ denotes the Frobenius norm.

The minimization problem can be solved using different ways such as QR-decomposition. Alternatively, we can use the Moore-Penrose pseudo inverse of **Y**. Using the right pseudo inverse $\mathbf{Y}^+$ of **Y** the coefficient matrix **A** can be solved by:

$$\mathbf{A} = \mathbf{E}_c\,\mathbf{Y}^+$$

To sum up, here are the different steps to estimate the spherical harmonics coefficient from far field measurements:

- Convert data from spherical to Cartesian coordinates system for all measurement points
- Compute the spherical harmonics matrix **Y**
- Compute the pseudo inverse $\mathbf{Y}^+$ of **Y**
- Compute the spherical harmonic coefficient matrix using $\mathbf{A} = \mathbf{E}_c\,\mathbf{Y}^+$

4. OBSERVATIONS AND DATA ANALYSIS

4.1. INTRODUCTION

The second measurement series aims to investigate the effect of the human phantom on antenna response placed on different distances from the antenna. Thomson 1 is used all along the measurement series 2. The purpose, here, is to study the evolution of antenna response with respect to the distance between the phantom and the antenna. The first section will be dedicated to some preliminary simulations about truncating the spherical harmonics basis and the compression task. In the second section, some observations concerning the antenna response will be shown and how the antenna pattern varies in the presence of the phantom at different distances. The last sections will present the variations in the space of spherical harmonics (modulus, energy and argument).

4.2. PRELIMINARY SIMULATIONS

4.2.1 SPHERICAL HARMONICS LEVEL

The spherical harmonics define a complete basis over the sphere and just as the Fourier Transform, the reconstruction is exact as long as the level goes to infinity. For that reason, we proceed to an approximation by limiting the maximum level to **L**.

The aim of these first simulations is to identify the best spherical harmonics level to reconstruct the antenna response. In fact, we look for the level giving the best tradeoff between the number of coefficient and the reconstruction error.

Figure 4-1 represents the relative reconstruction error of the antenna response with respect to spherical harmonics levels at different frequencies.

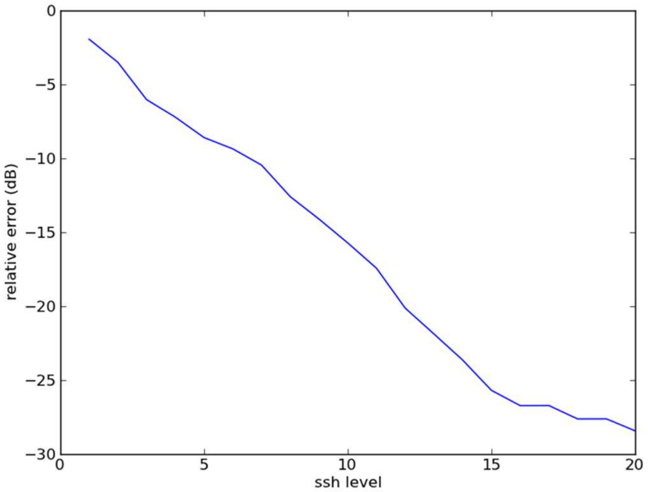

Figure 4-1: Reconstruction error evolution with respect to SH level

We notice that these results are consistent with the results of the paper [Rahola2009] and explain our choice of the level **L = 20**. This value has also been observed with vector spherical coefficient see Figure 3-1. Notice that maximum level value may change from an antenna to another.

4.2.2 DATA COMPRESSION

Before starting the data analysis task, we proceed to a compression task, in order to reduce the number of coefficient and better understanding the data.

The compression criterion is the modulus of the coefficient which is compared to a threshold that guaranties at the same time a good reconstruction and compression.

As the figure below shows, the threshold is fixed at **- 40 dB** and ensure an almost perfect reconstruction and very high compression rate, in fact, we reconstruct the antenna pattern with 42 coefficients.

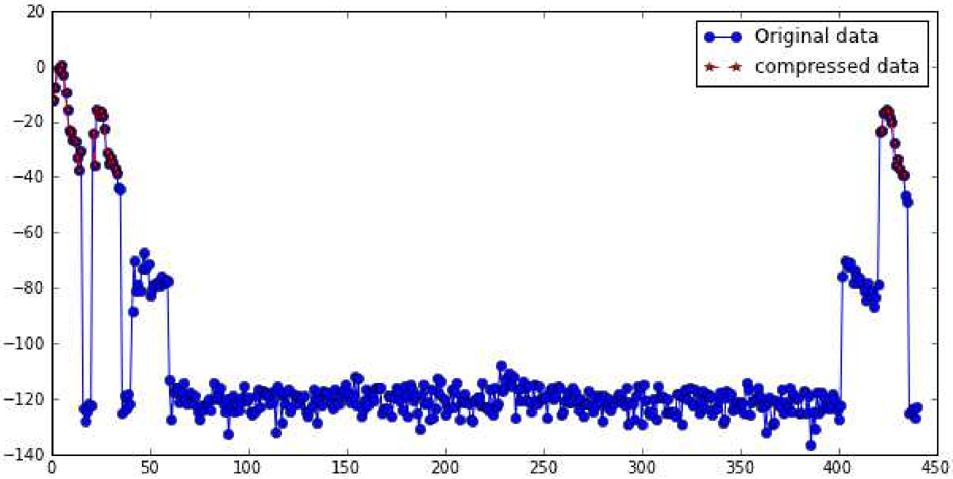

Figure 4-2 Data Compression

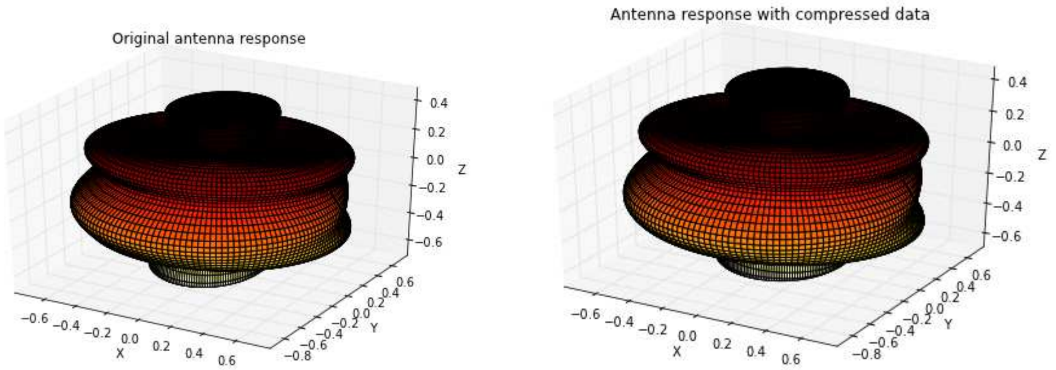

Figure 4-3 Antenna pattern with complete data (left) and with compressed data (right)

4.3. EVOLUTION OF THE ANTENNA RESPONSE AS A FUNCTION OF THE DISTANCE BETWEEN THE ANTENNA AND THE PHANTOM

In this section, we present the antenna response in the presence of the phantom and investigate how the antenna diagram varies. The following figures show the antenna radiation diagram at the frequency f **= 3.1 GHz** and for different distances from the phantom.

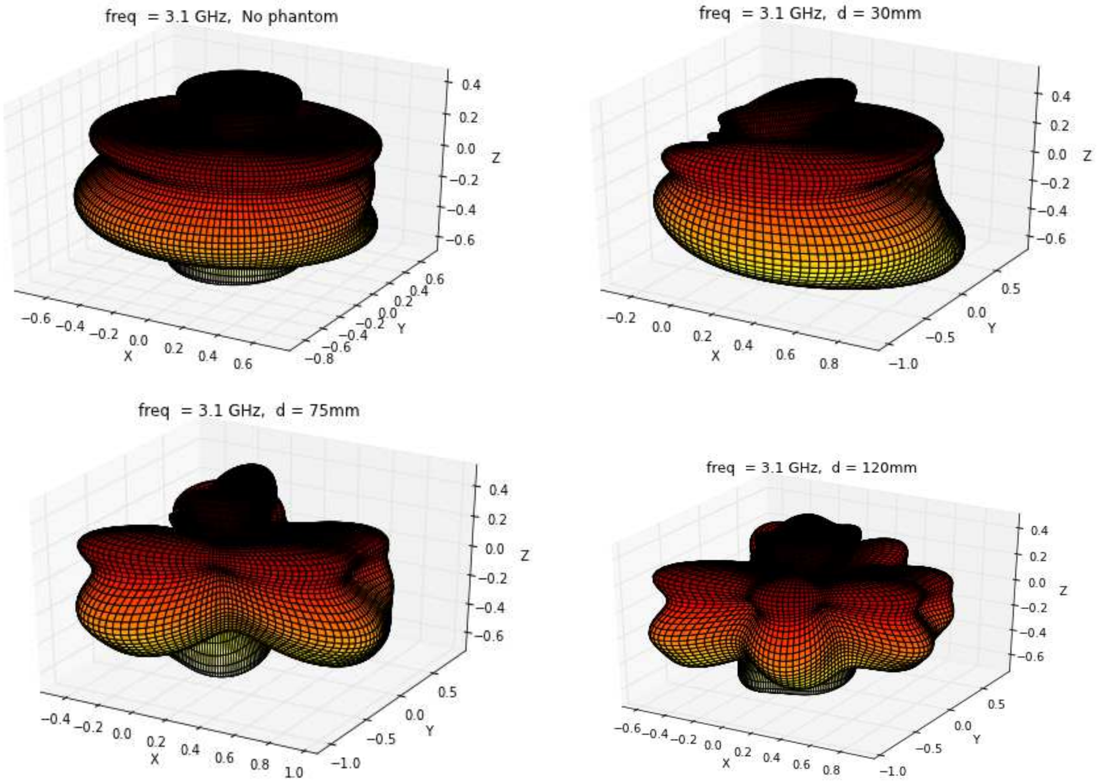
freq = 3.1 GHz, No phantom

freq = 3.1 GHz, d = 30mm

freq = 3.1 GHz, d = 75mm

freq = 3.1 GHz, d = 120mm

Figure 4-4 Antenna pattern for different distances of the phantom

As shown in the Figure 4-4, the presence of the phantom leads to:

- In very short distances: the antenna is directional and beams to one hemisphere.
- In larger distances: the antenna recovers, little by little, the omni-directional behavior, but it represents some ripples around the omni-directional case. This might be clearer in 2-D representation, in the figure below:

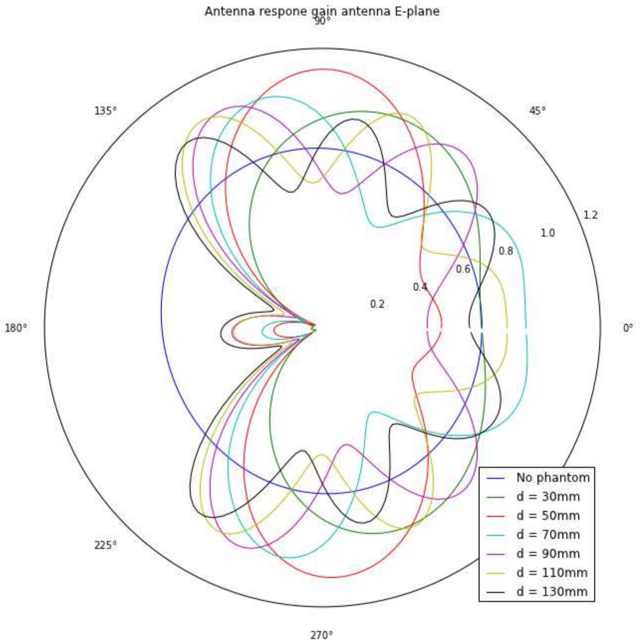

Figure 4-5: Influence of the phantom distance on antenna response gain

4.4. EVOLUTION OF THE SSH COEFFICIENT AS A FUNCTION OF THE DISTANCE BETWEEN THE ANTENNA AND THE PHANTOM

In this section, we will investigate the phantom presence effect on the spherical harmonics domain. The variation will be studied in terms of coefficients modulus and argument.

4.4.1 COEFFICIENT MODULUS ANALYSIS

This subsection is dedicated to present the spherical harmonics coefficients modulus and their evolution with respect to the distance between the antenna and the phantom.

Figure 26 represents the coefficient modulus with respect to index for different distances. Coefficients are indexed as follows: all the levels, mode 0; all the levels mode 1, etc …

$$m = [0,0,\ldots,0,1,1,\ldots,1,\ldots,L,-L,\ldots,-1,-1,\ldots,-1]$$

$$l = [0,1,\ldots,L,1,2,\ldots,L,\ldots,L,L,\ldots,1,2,\ldots,L]$$

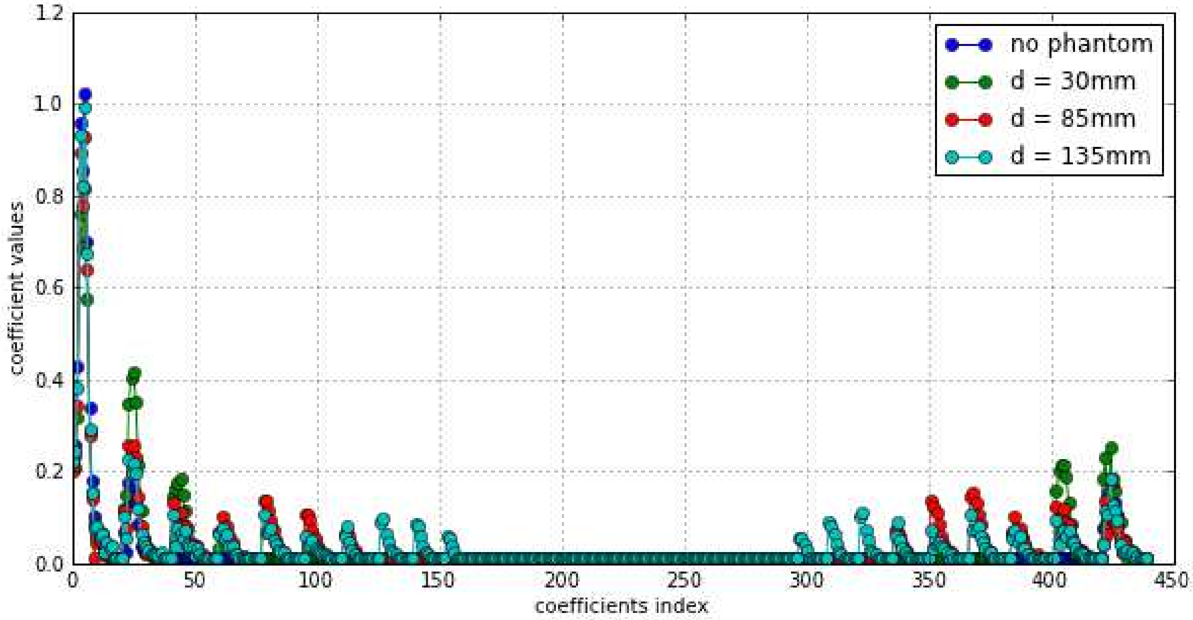

Figure 4-6 Evolution of SSH coefficient modulus w.r.t coefficient index

From the figure 26, it can be observed that the number of significant modes increases with the distance between the phantom and the antenna.
In fact, a mode m represents the number of circles passing through the poles, and this is consistent with the observations in the previous section, since we observe, in the radiation patterns, ripples around the omni-directional case which increase with the distance from the phantom. Therefore, we need more modes to represent accurately the antenna pattern.

Based on the measurement campaign, we notice that the number of significant modes varies proportionally with the distance between the antenna and the phantom, as the figure below shows.

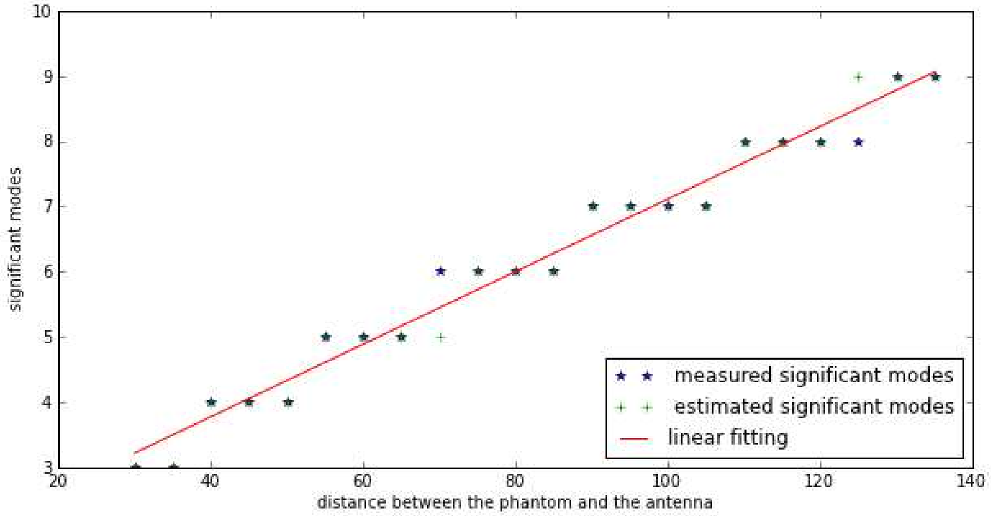

Figure 4-7: Number of significant modes

4.4.2 COEFFICIENT ENERGY ANALYSIS

In this part, the goal is to investigate the evolution of the coefficient energy with respect to the distance between the phantom and the antenna.

The figures below show the variation of the energy of different modes (m) and levels (l) with respect to the distance. We notice that:

- The total energy remains constant for different distance between phantom and antenna
- The different levels' energy remain almost constant for different distance.
- The most significant variation is on the modes' energy

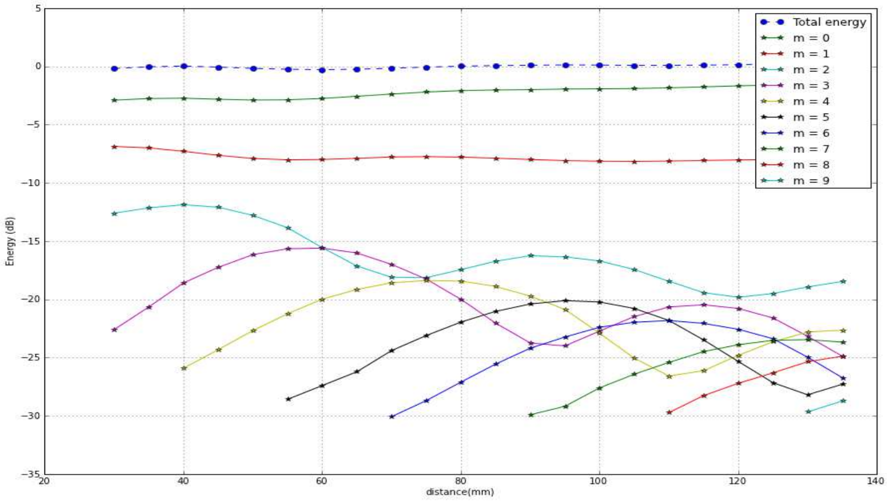

Figure 4-8 Evolution of mode energy with cylinder/antenna distance

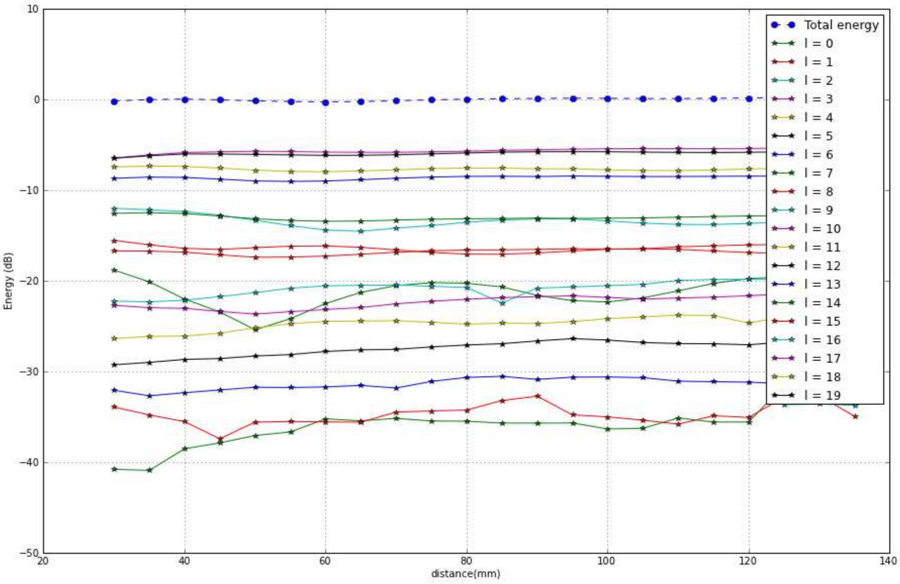

Figure 4-9 Evolution of level energy with cylinder/antenna distance

Analyzing the energy, the presence of the phantom at different distances has the most significant effect on the mode. This is due to the choice of this measurement series. The phantom is placed on the *x* axis of the antenna local frame, which affects the original symmetry around ϕ in spherical coordinates. Thus the variation is seen on modes and not on levels.

The most interesting about the mode's energy variation is that the higher one (|m|> 1) represents a shifted and mitigated copy of the first one(|m| = 1).

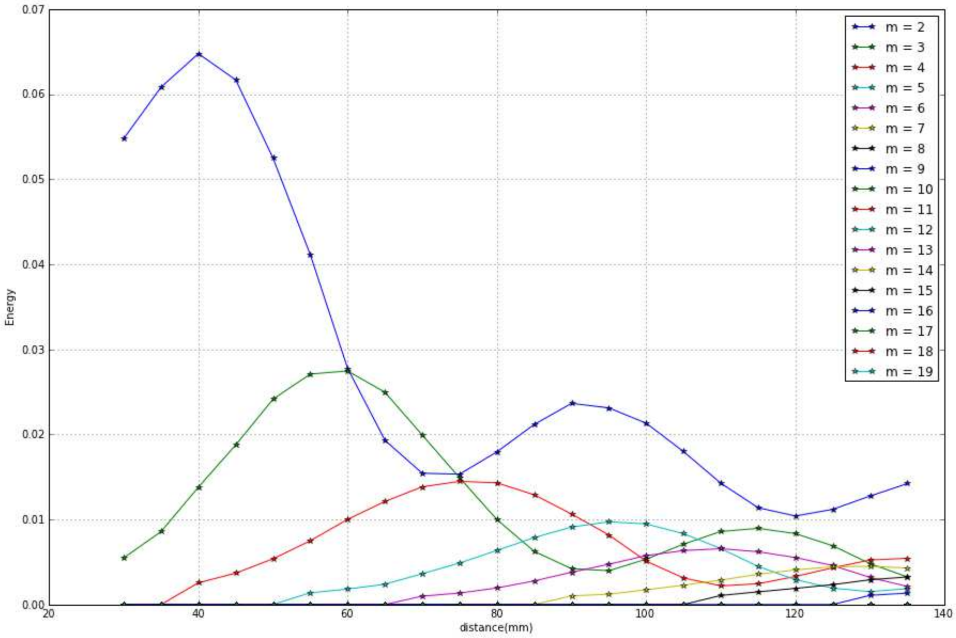

Figure 4-10 Evolution of mode's energy with phantom/antenna distance

The energy mitigation is presented in the Figure 4-11:

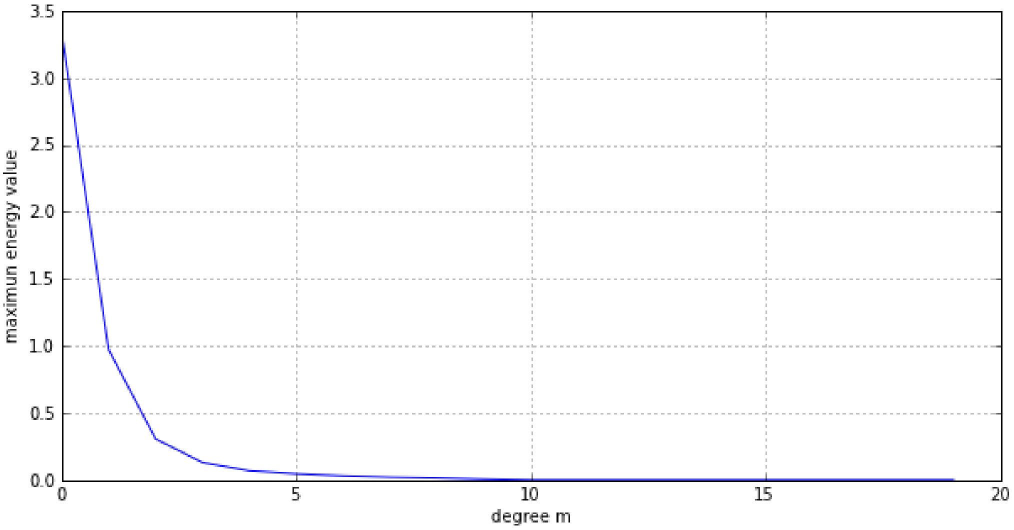

Figure 4-11: mode's energy mitigation as a function of the mode

4.4.3 COEFFICIENT ARGUMENT ANALYSIS

This subsection is dedicated to present the variation of the coefficient argument with respect to the distance between the antenna and the phantom. In fact the coefficient argument is the most delicate component, since a simple coefficients argument shift may change completely the beam direction.

As we can observe below, the coefficient argument variation is far from being random. As figures 30 below show, this variation depends on the mode m, for example, in first modes $m = [0, 1]$ the argument evolution with respect to the distance takes only two values: no phantom coefficient argument +0/π(the z component argument is presented, since it is the most significant).

On the other side, for higher modes we notice that we no more have a two values case. In fact, a certain shift is introduced on these arguments and this shift depends on both the distance and the mode (m)

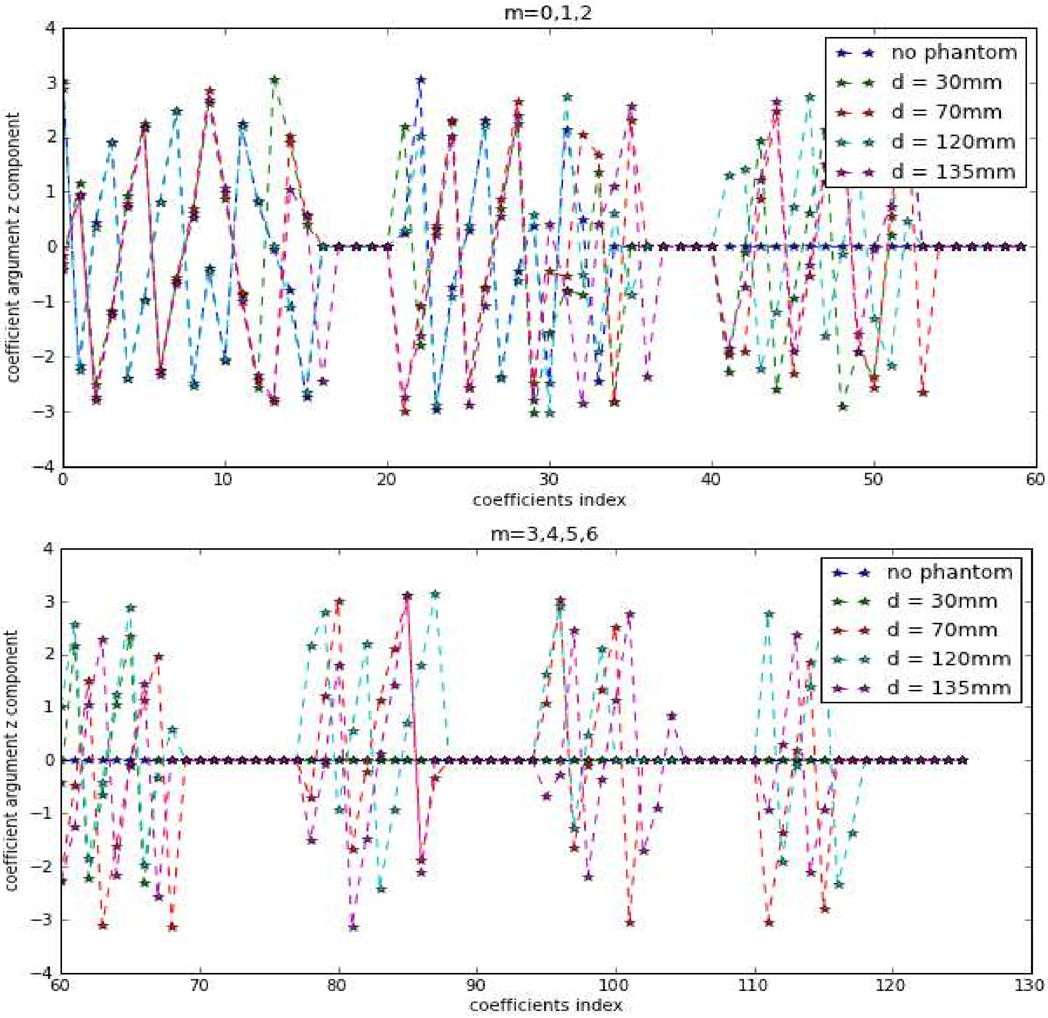

Figure 4-12: Z component argument

We can deduce that a coefficient argument may take *n* values, where *n* depends on the modes of the coefficient and as the histograms in Figure 4-13 show, the coefficient argument are much more scattered when the mode *m* increases.

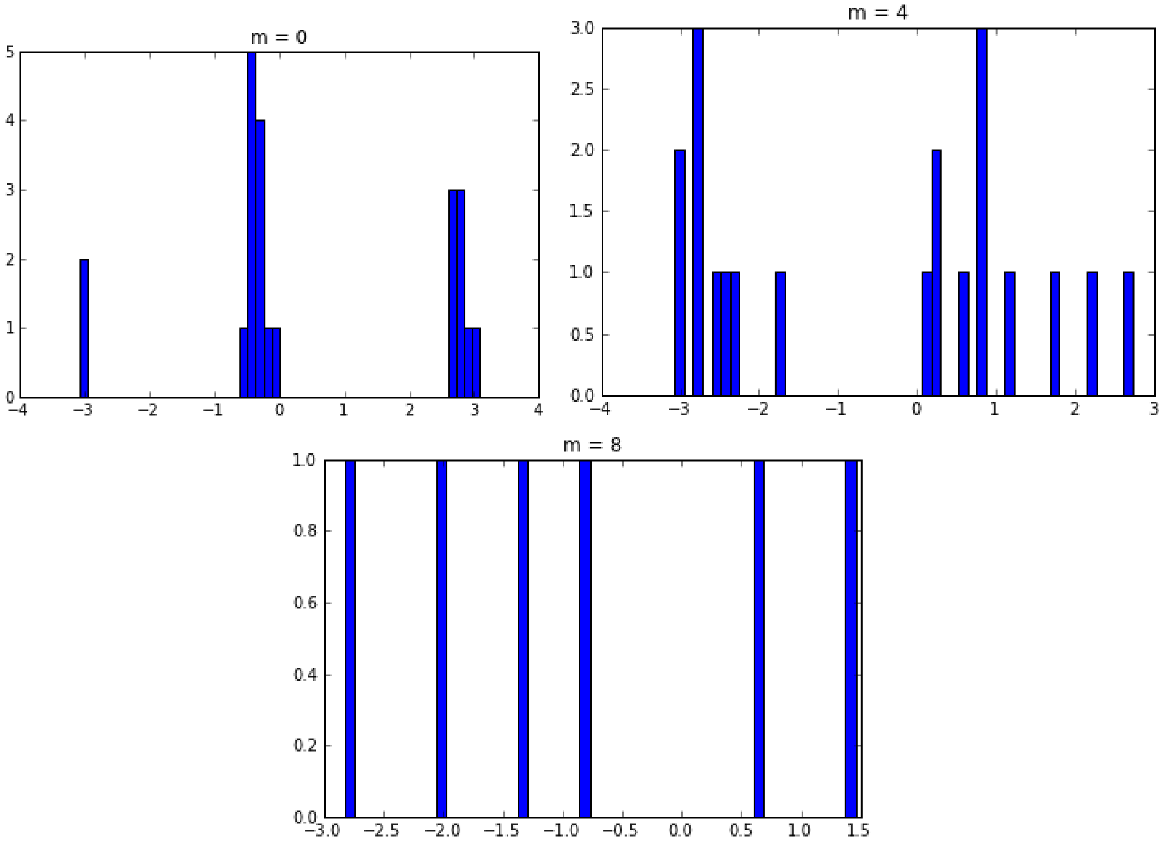

Figure 4-13 : Coefficient's argument for different modes m

5. MODELING THE PHANTOM EFFECT ON SSH COEFFICIENT

The current section refers in a first subsection 5.1 to the preliminary work made to derive a first model to predict the behavior of the SSH coefficient with respect to the distance between antenna and phantom extracted from the Series 2 of the measurement campaign. In a second subsection, a preliminary geometrical model, which is an extension in three dimension of a classic problem described in [McNamara1990]

5.1. MODELING THE PHANTOM EFFECT ON SSH COEFFICIENT

5.1.1 INTRODUCTION

The spherical harmonics is an efficient way to store data relative to antenna pattern, especially when antenna is taken into account in a propagation channel simulator such as ray tracing. After optimizing the storage of antenna pattern, the goal of this part is to model the variation of the spherical harmonics coefficients with the distance of the human phantom introduced in a previous part. In fact, we aim to, knowing the SH coefficients of an antenna, predict the coefficient in the presence of the phantom at a distance d

$$\tilde{C}_{l,m}(d) = \mathrm{f}(C_{l,m},\mathrm{d})$$

where $\tilde{C}_{l,m}(d)$ is the coefficient of level l and mode m in the presence of the phantom at the distance d and $C_{l,m}$ is the coefficients representing the original antenna.
To achieve that goal, we deal with the coefficient modulus and arguments separately.

5.1.2 COEFFICIENT MODULUS SYNTHESIS

As mentioned before, the presence of the human phantom causes the emergence of higher modes to represent the ripples in the antenna pattern. In fact, a dipole antenna is, traditionally, represented by the modes $m = [0,1]$, and in the presence of the human phantom these two modes are not sufficient anymore and the number of modes increases with the distance.
The first modeling step is to determine the number of necessary modes to represent the antenna pattern. To do that, we use the linear fitting illustrated in Figure 4-7 in subsection 4.4.1

$$M(d) = \lceil ad + b \rceil$$

where ⌈ ⌉ is the ceil integer part, d is the distance of the phantom, a and b are the linear fitting parameters.
Once we have the number of modes $M(d)$, we start modeling the coefficients and we start with the permanent modes (modeling the original antenna $m = [0,1]$)

- **m = 0**

The fundamental mode *m = 0,* is the one representing the sphere and as a consequence the omni-directional aspect. For this reason and in terms of energy, this mode falls in the presence of the phantom and increases with the distance since we recover little by little the omni-directional behavior (Figure 5-1).

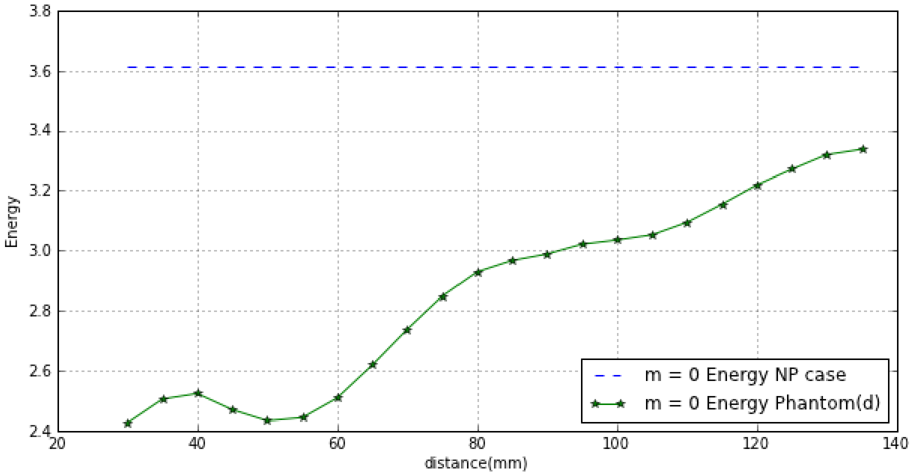

Figure 5-1: Mode m= 0 Energy

But in terms of coefficient, it is not the case for all components:

- Z Component varies identically as the total mode energy and this variation is modeled linearly as:

$$\left|\tilde{C}_{l,0}^{z}(d)\right| = \left(1 - \alpha_0^z \frac{d_{lim} - d}{d_{lim}}\right)\left|C_{l,0}^{z}\right|$$

where d_{lim} is a large distance from which the phantom has no effect and the antenna pattern requires the original behavior which is fixed at *1000 mm* and $\alpha^z > 0$.

The Figure 5-2 and Figure 5-3 represent the modeling of the z component coefficient for two different distances

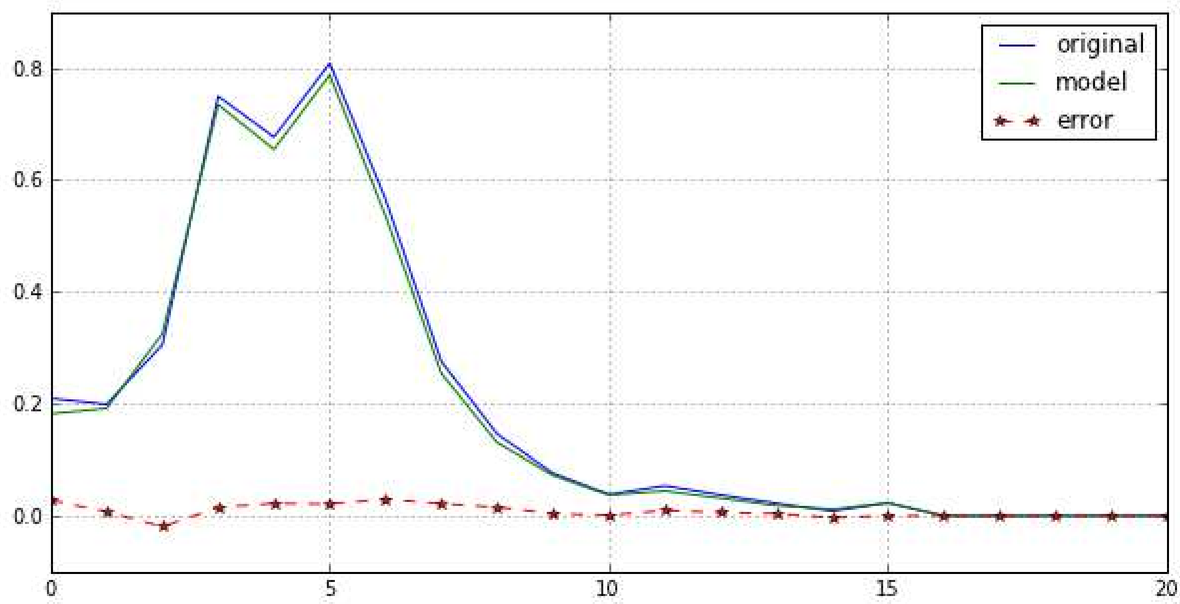

Figure 5-2: Z component Modeling at d =30

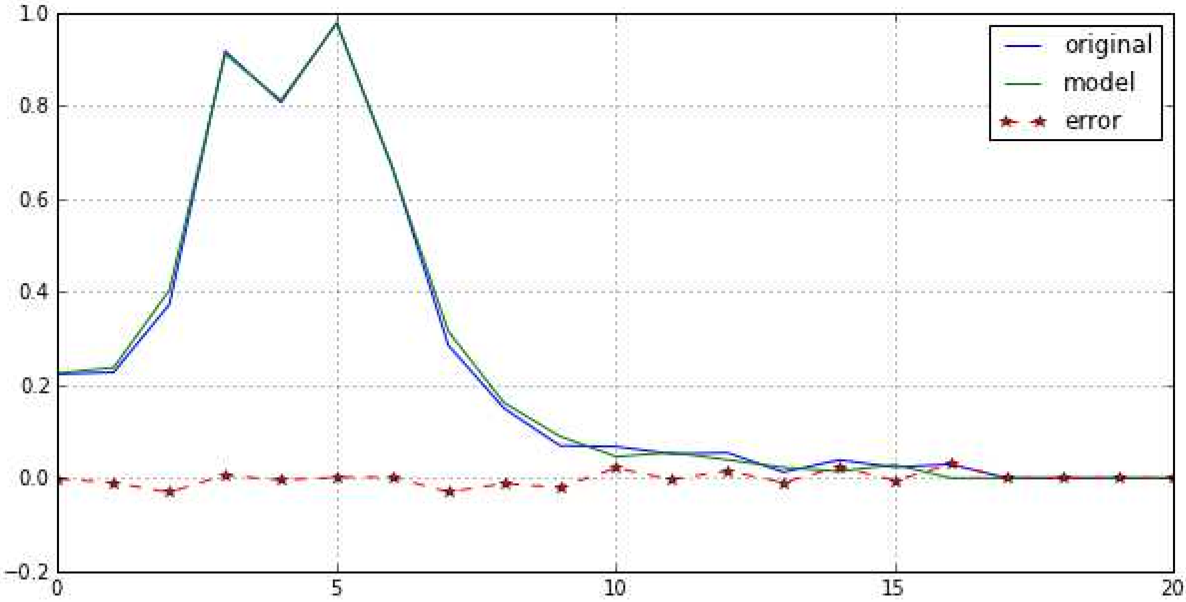

Figure 5-3: Z Component modeling at d = 130

- X component varies inversely to Z because of the antenna position on the X axis

$$\left|\tilde{C}_{l,0}^{x}(d)\right| = (1 - \alpha_0^x \frac{d_{lim} - d}{d_{lim}})\left|C_{l,0}^{x}\right|$$

- Y component remains the same as no phantom case

$$\left|\tilde{C}^{y}_{l,0}(d)\right| = \left|C^{y}_{l,0}\right|$$

- **m = 1**

The mode *m = 1* is the one representing the monopole aspect and for that reason the coefficient modulus are maximum when the phantom is too close and decrease with the distance to require the dipole aspect.

$$\left|\tilde{C}^{x,y,z}_{l,1}(d)\right| = (1 - \alpha^{x,y,z}_{1}\frac{d_{lim} - d}{d_{lim}})\left|C^{x,y,z}_{l,1}\right|$$

- **m > 1**

These coefficients are the ones appearing because of the existence of the phantom and based on the modes energy variation presented previously (the modes energy m>0 vary following the same way), the idea was to assign to these new coefficient a mitigated copy of the highest permanent mode in our case (m =1) and following the same mitigation in Figure 4-11. The maximum energy of each single mode m is obtained empirically from a linear fitting of the maximum energy as a function of distance $E_m(d)$ in log scale extracted from the series 2 data.

$$E^{max}_{m} = \max_{E} E_m(d) = \beta e^{-\gamma m}$$

In the case of the serie 2 fitting one obtain β≈3.25 and γ≈1.08. Those values are specific to a single dataset and should be later considered as random variables whose distribution should be determined. This would necessitate to realize other measurement series to investigate the variability of those coefficients with respect to various parameters as antenna type and phantom dimensions and dielectric characteristics. Unfortunately the last measurement series performed in January 2013 are unreliable after a long breakdown period and was unable to answer this addressed question.

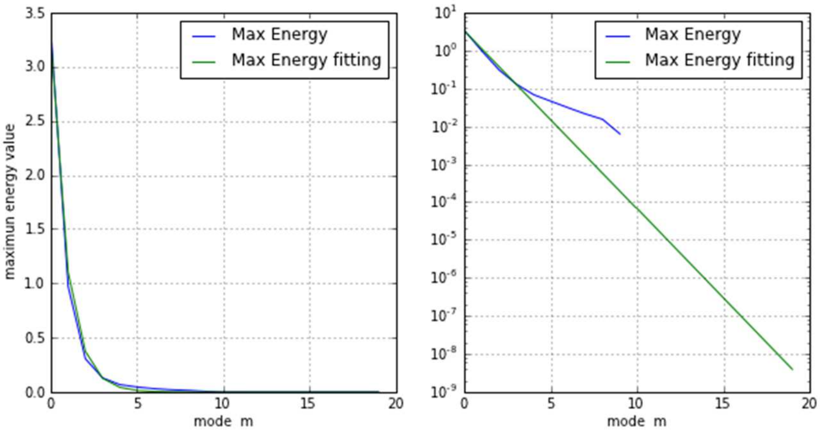

Figure 5-4: Max total energy (all components) fitting from series 2 data

The next figures shows the models results. In fact the Figure 5-5 and Figure 5-6 represent the coefficients value resulting from the model and compare them to the original ones:

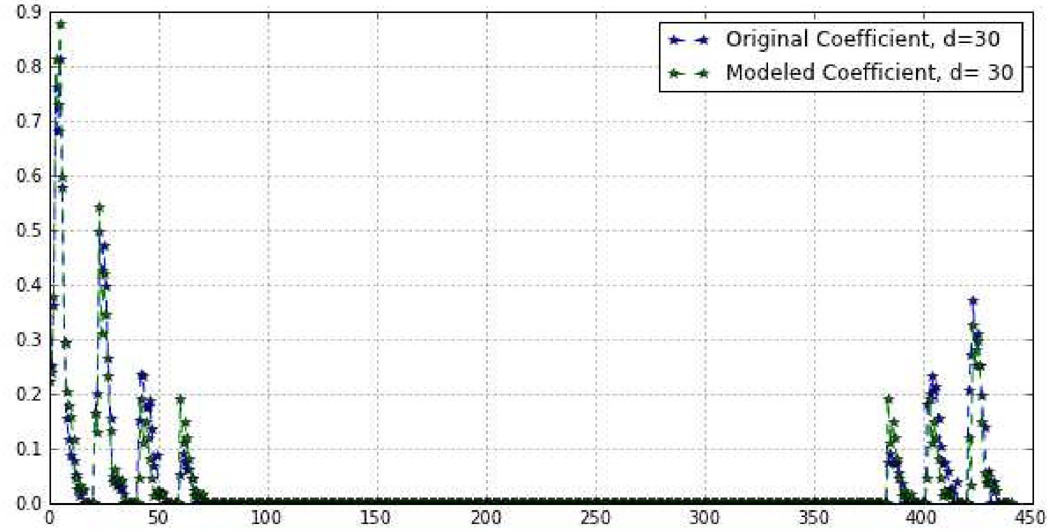

Figure 5-5: Modeled vs Original coefficient at d = 30

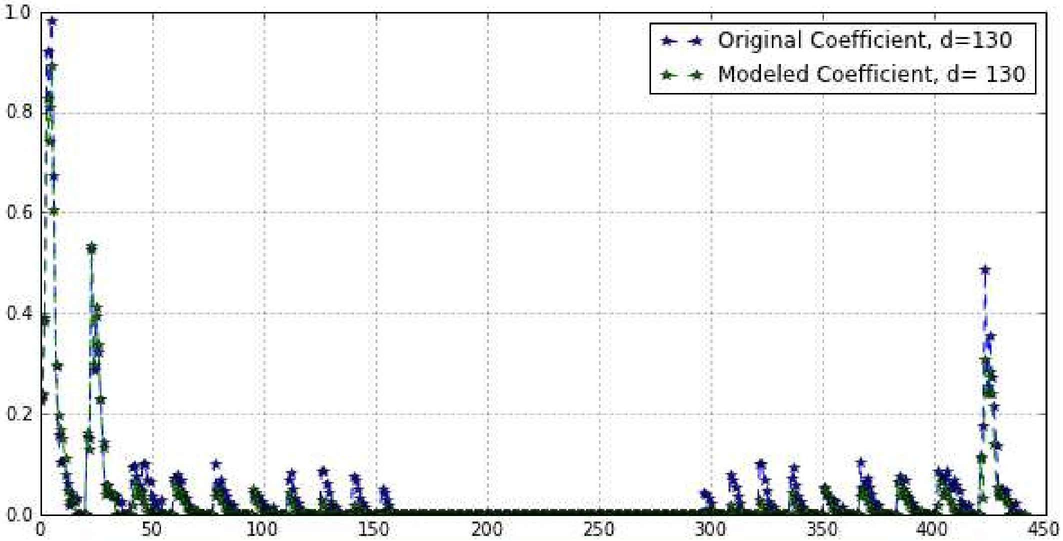

Figure 5-6:Modeled vs Original coefficient at d =130

The next figure represents the average of the coefficient modulus error for the different distances.

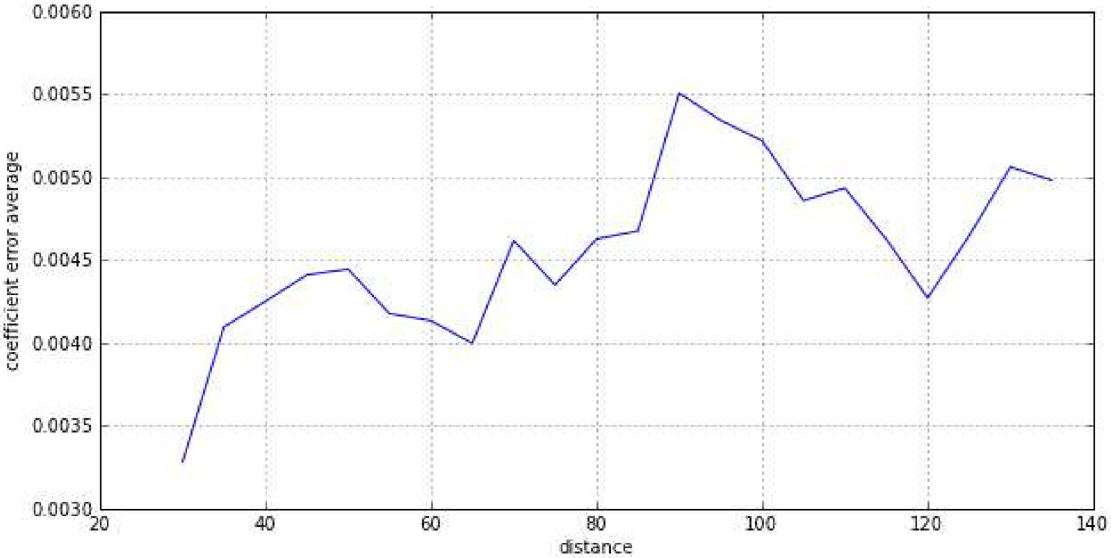

Figure 5-7: Error average of the coefficient value

In order to check the reconstruction pattern and whether the coefficient value model is acceptable, we assign to the modeled coefficients the real argument and show the antenna patterns.

Those presented results mean that provided the argument is known (genius aided situation), the proposed coefficient modulus model as a function of the distance allows to synthesize a realistic useable pattern for BAN simulation. Unfortunately, the analysis of the argument do not provide a simple linear as for the modulus. However, obviously, there is some hidden rule behind the observed data.

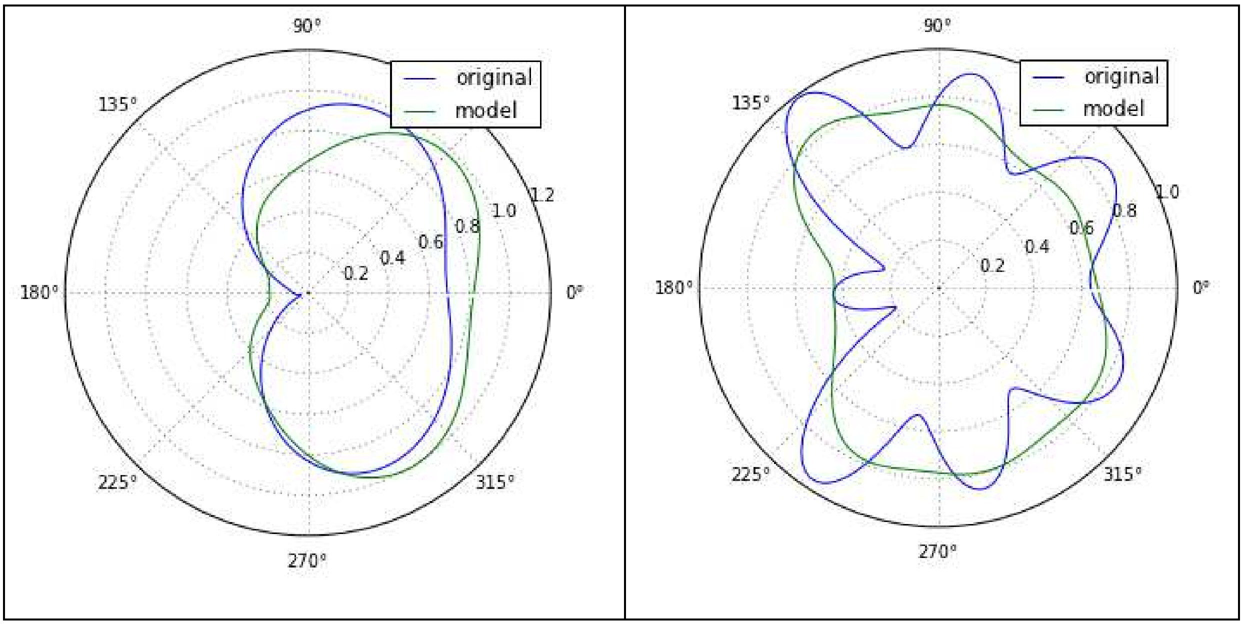

Figure 5-8: Antenna Pattern in the plan θ = 90 at d = 30, 130

The whole antenna pattern is presented by Figure 5-9 and Figure 5-10.

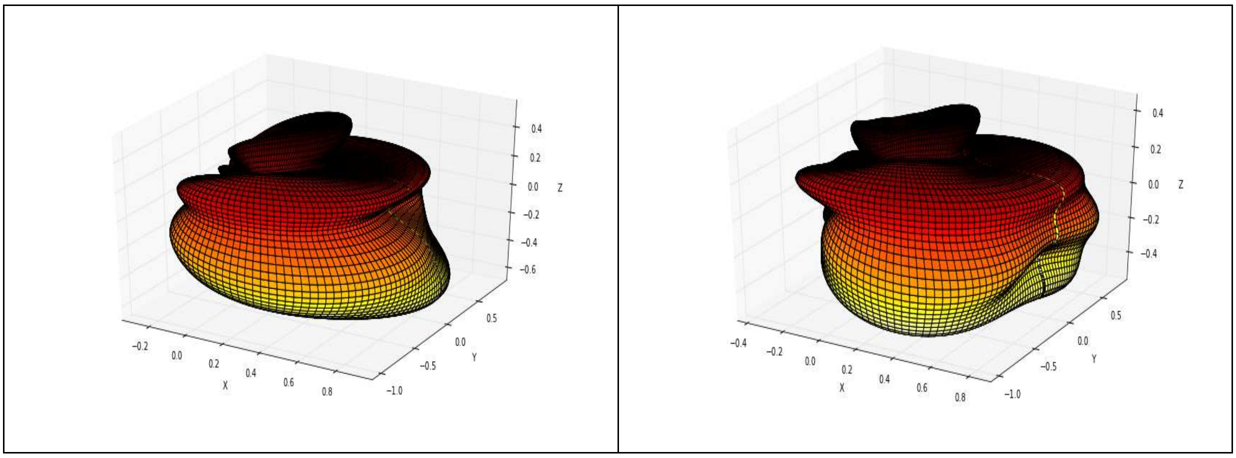

Figure 5-9: Original and Modeled Antenna pattern at d = 30

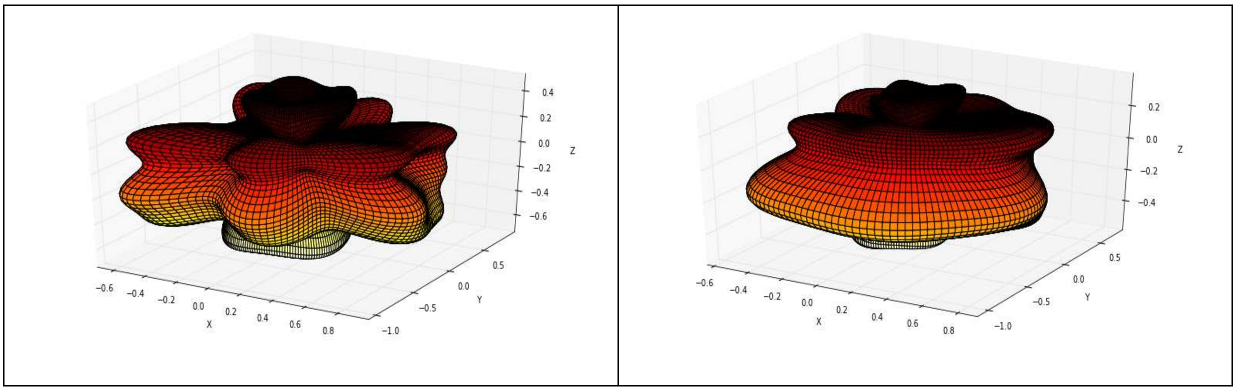

Figure 5-10: Original and Modeled Antenna pattern at d =130

5.2. FORMULATION OF A 3D ADDITIVE MODEL

The first approach which has been envisaged was a dead end and it was not really possible to generate any exploitable pattern because the understanding of the phase structure was not clear.

Very recently the problem have found a new way based on the idea to exploit a 3D adaptation of a canonical problem of reflection of a radiation by a line source which is described in the book of Mac Namara on uniform theory of diffraction. This simple additive model is able to capture the very nature of the problem which is that in the far field the total field is obtained as the sum of two phase shifted contributions.

- The contribution of the primary source.
- The contribution of the reflected source.

The first observation of the data in the spherical harmonics domain has convinced us that we should seek a model for explaining the structure of the phase of the coefficient. This understanding is quite recent and we are still in the process to formulate the model. In the following are given the very elements which largely inspired from the classical book of Mac Namara. The novelty here comes from the 3D formulation and of course the very context of utilization of the model.

The purpose of the model following is to take into account the presence of a dielectric cylinder in the immediate proximity of an electromagnetic source. Let's consider in a first approach that the source is a line source and that the cylinder is infinite along the z axis.
The model is additive meaning that it uses the unperturbed antenna, which can be measured or simulated, and two fundamental parameters, a the radius of the dielectric cylinder and b the distance between the line source and the center of the cylinder which is also the origin of the canonical problem. The distance between the cylinder and the source is $d=b-a$.

The geometry of the problem is described in Figure 5-11.

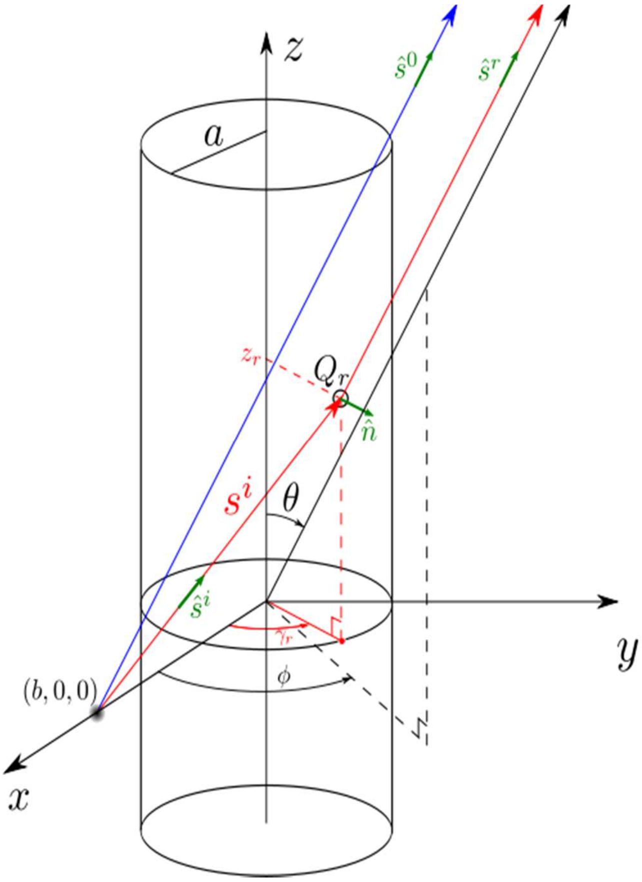

Figure 5-11 Geometry of the canonical problem

The unitary vector along the far field direction of observation is given by:

$$\hat{s} = \cos\phi \sin\theta\, \hat{x} + \sin\phi \sin\theta\, \hat{y} + \cos\theta\, \hat{z}$$

The unit vector in the direction from the source point $S(b,0,0)$ to the reflection point $Q_r(a\cos\gamma_r\ , a\sin\gamma_r\,, z_r)$ is given by

$$\hat{s}^i = \frac{(a\cos\gamma_r - b)\,\hat{x} + a\sin\gamma_r\,\hat{y} + z_r\hat{z}}{(a\cos\gamma_r - b)^2 + (a\sin\gamma_r)^2 + {z_r}^2}$$

The cylinder normal in Q_r is given by:

$$\hat{n}(Q_r) = \cos\gamma_r\,\hat{x} + \sin\gamma_r\,\hat{y}$$

$$\hat{n}.\hat{s}^i = \frac{a - b\cos\gamma_r}{\sqrt{a^2 + b^2 - 2ab\cos\gamma_r + z_r^2}}$$

So the dot product

$$\hat{n}.\hat{s}^{r} = \cos(\phi - \gamma_r)\cos\theta$$

Enforcement of the reflection law

$$\hat{n}.\hat{s}^{r} = \hat{n}.\hat{s}^{i}$$

Then yields the following transcendental equation for the determination of the stationary point parameterized by γ_r and z_r

$$\frac{a - b\cos\gamma_r}{\sqrt{a^2 + b^2 - 2ab\cos\gamma_r + z_r^2}} = \cos(\phi - \gamma_r)\cos\theta$$

5.2.1 DETERMINATION OF THE REFLECTION CAUSTIC DISTANCE

The radius of curvature of the incident wavefront at Q_r

$$s^i = \sqrt{a^2 + b^2 - 2ab\cos\gamma_r + z_r^2}$$

5.2.2 DIRECT FIELD AT OBSERVATION POINT IN THE FAR FIELD

$$s^r = s - a\cos(\phi - \gamma_r)\sin\theta$$

$$s^0 = s - b\cos\phi\sin\theta$$

The antenna not perturbed by the cylinder has the following vector radiation pattern

$$U^i = (F_\theta(\theta,\phi)\hat{\theta} + F_\phi(\theta,\phi)\hat{\phi})\frac{e^{-jks^0}}{\sqrt{s^0}}$$

5.2.3 INCIDENT FIELD AT THE REFLECTION POINT

Let Q_r be the reflection point on a infinite cylinder. The incident field in Q_r is given by :

$$U^i(s^i,\theta_r,\phi_r) = (F_\theta(\theta_r,\phi_r)\hat{\theta}_r + F_\phi(\theta_r,\phi_r)\hat{\phi}_r)\frac{e^{-jks^i}}{\sqrt{s^i}}$$

$$\frac{1}{\rho_r} = \frac{1}{\sqrt{a^2 + b^2 - 2ab\cos\gamma_r + z_r^2}} + \frac{2}{a\cos(\phi - \gamma_r)}$$

This approach is not an exact formulation of the diffraction by an infinite dielectric cylinder. This choice has been made here because the BAN context does not require knowing an exact solution because there is very much other source of high variability. The objective is to capture into the model the very nature of the phase variation in order to preserve the realism of synthesized pattern. We are also currently considering going to a more exact but also more complex formalism which would be valid in all space including the shadow region. It is not straightforward at that point to say if this extra realism would worth.

6. ON-BODY ANTENNAS FOR CHANNEL MEASUREMENTS: EVALUATION BY EM SIMULATIONS

In this chapter we present some of the antennas that have been or will be employed for channel measurement in the scope of T2.2. Their behavior on the body has been simulated by means of EM simulations. Different bodies have been considered: homogenous flat or cylinder phantoms and SAM phantom. These simulations are complementary to the measurements performed and will allow further analysis in the scope of T2.2 and T2.3.

6.1. WIDEBAND PLANAR MONOPOLE WITH INTEGRATED BALUN

The starting point of the antenna design is a classical notch antenna with reduced ground plane. Nevertheless the reduction of the ground plane yields to a radiating behaviour similar to a short-circuited printed dipole antenna. Thus the ground plane acts as dipole arms at $\lambda/2$. Since the printed dipole presents a relatively small bandwidth, the notch design has been modified in order to achieve wideband behaviour. This is obtained by means of an elliptical shape of the dipole arms, which results into a larger notch.

As a consequence the wideband impedance matching is obtained by combining two different antenna modes: in the first octave the antenna acts as a dipole, with omni-directional characteristics in the azimuth plane; while at highest frequencies the notch acts as an aperture antenna with small directive characteristics.

Additional antenna size reduction is obtained by folding up the dipole arms, which leads to a miniaturization factor of $\lambda/5$ instead of $\lambda/2$. A prototype has been realized on FR4 substrate of 0.8 mm thickness at CEA.

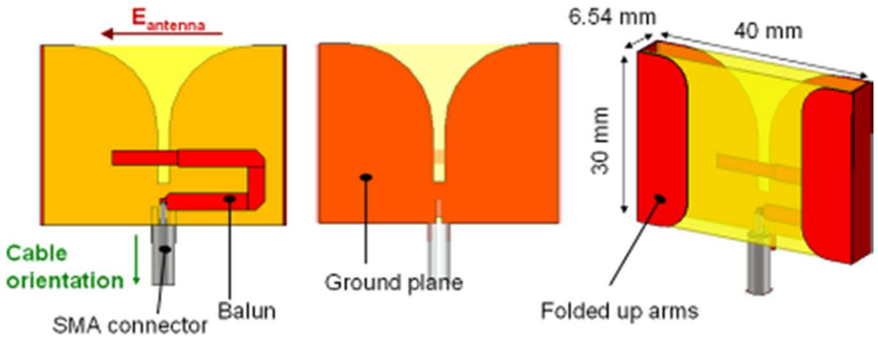

Figure 6-1 Antenna design

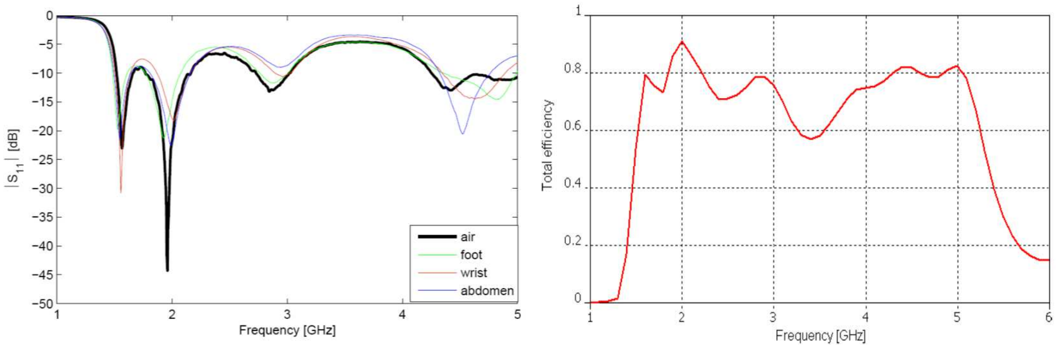

Figure 6-2: Antenna S11 (left) and total efficiency (right).

The antenna reflection coefficient has been measured in "on-air" and "on-body" conditions, as depicted in Figure 6-2. This antenna was originally designed to work in the 1.5–3.1 GHz band (|S11| <-7dB). Nevertheless it can be employed up to 5 GHz if a slightly higher mismatch can be accepted (|S11| < -6dB), since the antenna presents good performance in terms of total efficiency. Figure 6-2 shows a total efficiency larger than 75 % in the 1.5–5 GHz, with except of a small dip at 60 % in the 3.2–3.7 GHz band.

One of the main issues in small antenna characterization is the influence of the RF cable. This parasitic effect can greatly affect the channel characterization. To avoid these phenomena, this design presents a Balun structure, which allows the use of a SMA connector placed on the plane of the dipole structure. At the same time the SMA connector and RF cable orientation are orthogonal to the antenna radiated field, thanks to the Balun design.

A cable-less test-bed has been set up to characterize the radiation pattern of small antennas. The test bed is based on a fibre optic link. A Transmitter Optical Sub-Assembly converts RF signal to an optical one. Then a Receiver Optical Sub-Assembly converts the optical signal into a RF feed to the Antenna Under Test.

The angle-dependent transfer function, $H(f,\theta,\phi)$, of the antenna has been measured by using the optic link and the classical RF cable, in order to highlight the influence of the parasitic effect due to the cable.

Given the large bandwidth of the antenna, the Mean Realized Gain (MRG) computed in the azimuth plane. Figure 6-3 shows the MRG measured with both methods for two different bandwidths: from 1.5 GHz to 3 GHz and from 1.5 GHz to 5 GHz. The antenna presents good omni-directional characteristics in both bands. Nevertheless the poor impedance matching at higher frequencies yields to a slight gain decrease, as observed in Figure 6-3b.

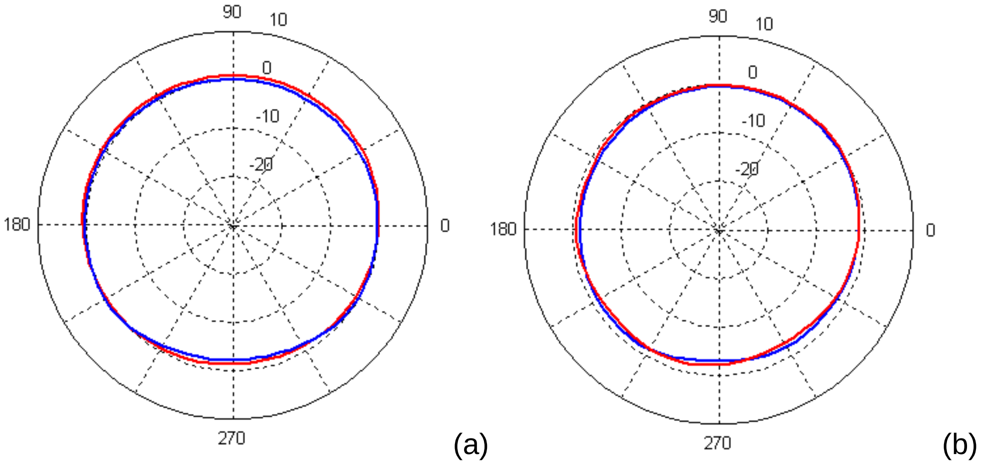

Figure 6-3: Mean Realized Gain: (a) [1.5-3] GHz, (b) [1.5-5] GHz. Measure with RF cable (blue) and optic link (red).

The most important outcome is that the differences between the RF cable and optic link measurements are practically irrelevant. This result shows that the antenna is notably a good candidate for on-body channel sounding, avoiding RF cable parasitic effect.

A second Planar (PL) monopole has been designed without folding the dipole arms (Figure 6-4).

This antenna, realized on FR4 substrate, presents 25x35x0.8 mm3 dimensions and its impedance matching band is 2.22-5.06 GHz, with respect to S11<-6dB. The antenna presents a quasi-omnidirectional behaviour as the previous antenna, and 70% total efficiency on the air at 2.4 GHz. This antenna has been employed in the second measurement campaigns at CEA. The antenna behaviour has been also simulated on the body. Results are not reported here for sake of briefness.

Figure 6-4 Planar Monopole antenna

6.2. TOP-LOADED MONOPOLE

A wide band top loaded monopole has been designed to investigate on-body channel by considering a polarization normal to the ground plane. The antenna is fed by a stripline on Roger 4003 substrate. This feeding allows the use of coaxial cables normal with respect to the main antenna polarization, and minimizes its influence on channel measurements. The antenna height is 11.5 mm and the ground plane is 50mmx50mm. Antenna design and prototype are shown in Figure 6-5.

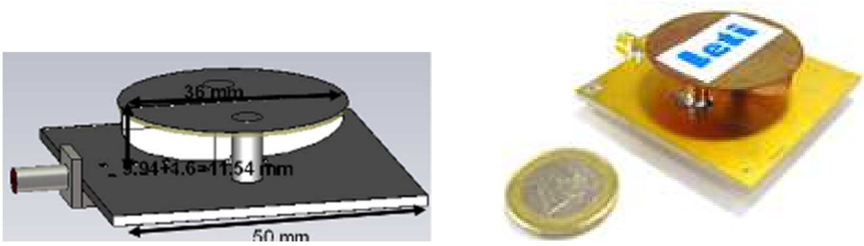

Figure 6-5: Top loaded monopole antenna

Measurement results show that reflection coefficient is below -7 dB over a very large bandwidth from 2.33 GHz up to 11 GHz, so that both 2.4 GHz and UWB can be investigated by using this antenna.

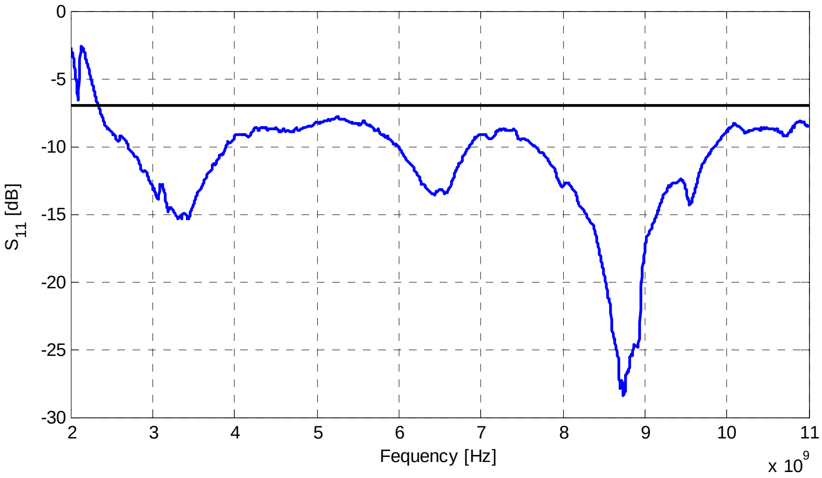

Figure 6-6: Atnenna return loss

A human homogenous body phantom (εr=41,σ=0.7 S/m) has been considered in simulation. Simulation results show that total efficiency is at least 70% from 2.36 to 5 GHz.

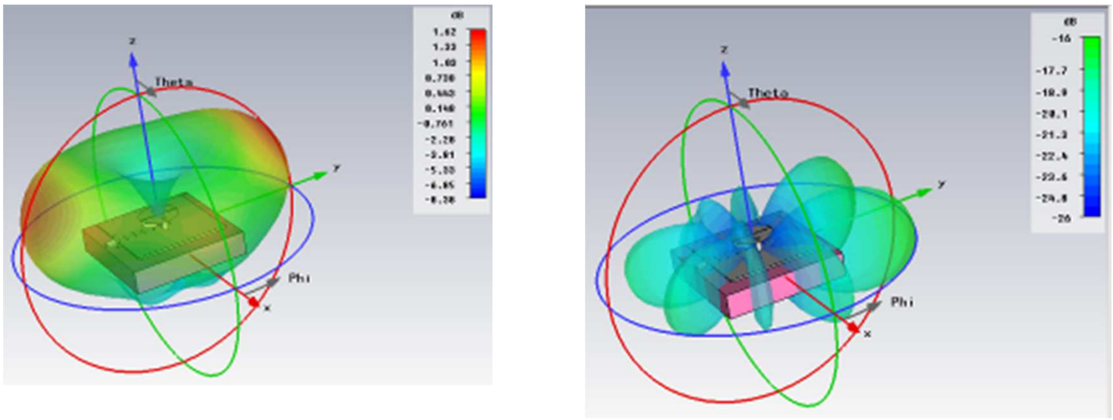

Figure 6-7: Antenna realized gain at 2.4 GHz on body: main polarization (left) cross-polarization (right)

Further simulations have been performed by using the SAM phantom [SAM_standards] in order to evaluate the antenna performance on the body. In Figure 6-8 we show the gain pattern of the TLM on the ear at the different frequencies.

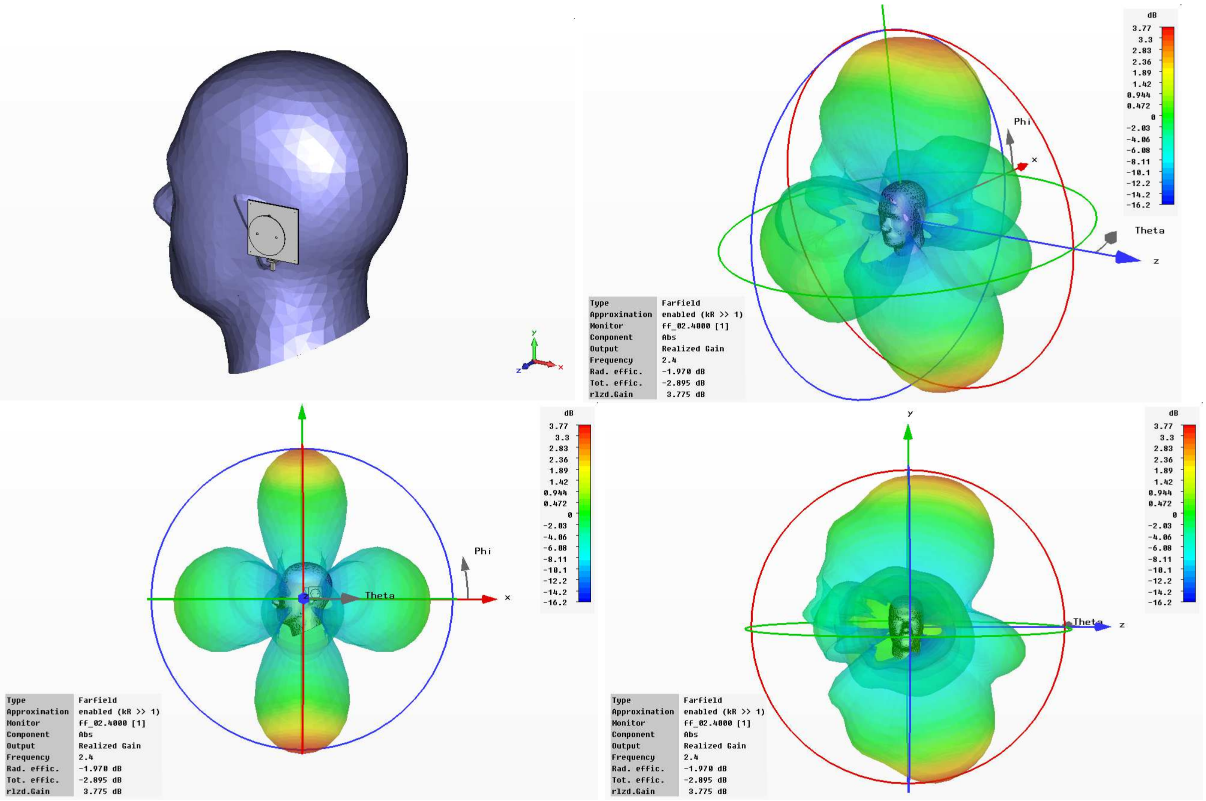

Type Farfield
Approximation enabled (kR >> 1)
Monitor ff_02.4000 [1]
Component Abs
Output Realized Gain
Frequency 2.4
Rad. effic. -1.970 dB
Tot. effic. -2.895 dB
rlzd.Gain 3.775 dB

Figure 6-8 Top-loaded Monopole on SAM head

6.3. ULTRA-WIDEBAND PRINTED CIRCULAR DIPOLE ANTENNA

The UWB printed circular dipole antenna presented in [Thom] and measured in the previous sections has been simulated CST Microwave Studio®. The realized gain pattern of the isolated antenna is presented in Figure 6-9 for different frequencies. The same antenna has been simulated with a cylinder homogenous phantom considering a radius of 30 cm and an antenna-body separation of 5 mm. The gain patterns of the antenna in the presence of the body at 3, 4 and 5 GHz are presented in Figure 6-10. The presence of the phantom strongly affects the antenna gain pattern. This effect should be considered when using ray-tracing model for off-body and body-to-body channels. The advantage of such simulations is the possibility to easily change the phantom characteristics (dimensions, permittivity, conductivity) and the antenna position and orientation with respect to the body, in order to take into account the variability of the antenna performance on the body.

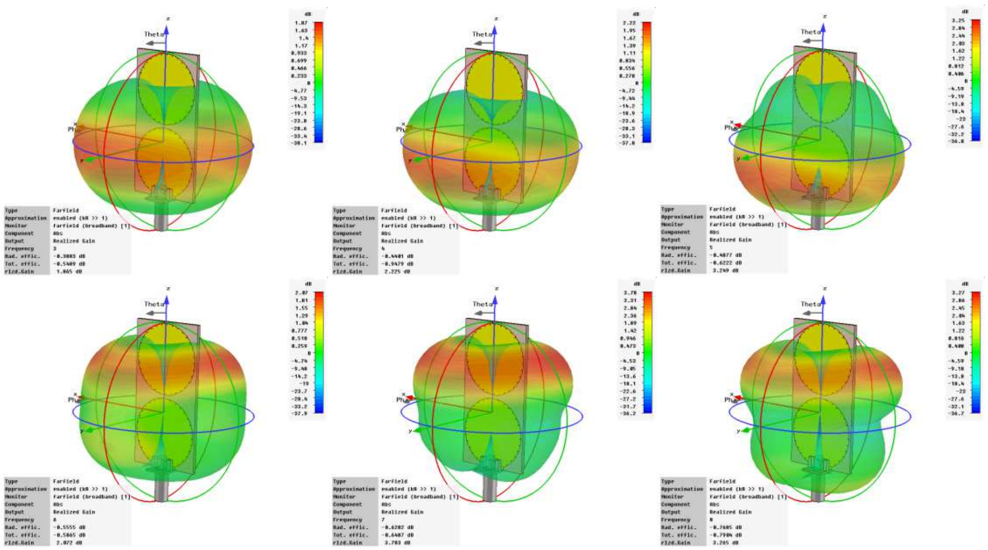

Figure 6-9 UWB printed dipole gain pattern at different frequencies

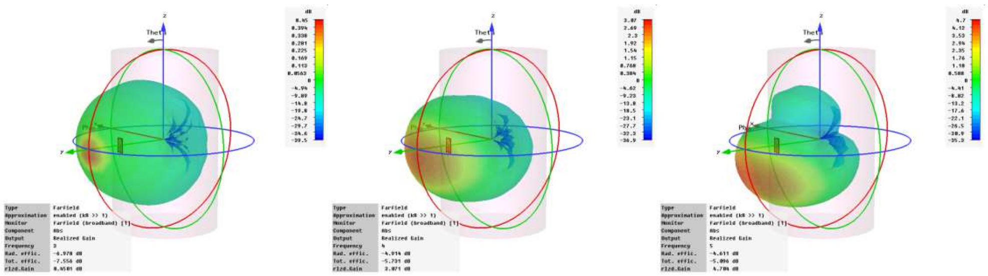

Figure 6-10 Gain pattern at 3, 4 and 5 GHz of the UWB printed dipole in the presence of an homogenous phantom

6.4. A SIMPLIFIED CASE STUDY

In addition to the antenna used for channel characterization, a simple case study has been considered. A half-wavelength dipole at 2.4 GHz has been simulated at different distances from a cylinder phantom. With respect to the classical donut-like pattern of the isolated antenna (Figure 6-11) the gain pattern in the presence of the body is strongly dependent on its separation from the phantom, as depicted in Figure 6-12. This is as an example of small database that can be extended and exploited for antenna-channel joint analysis.

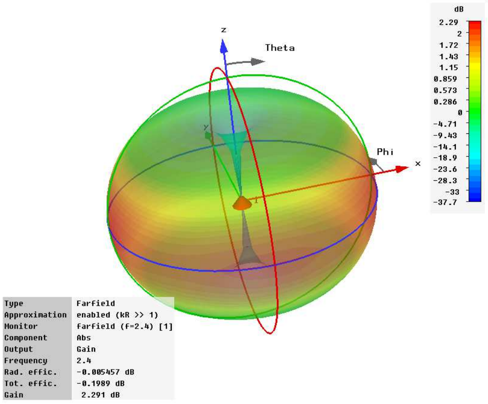

Figure 6-11 Half-wavelength dipole gain pattern

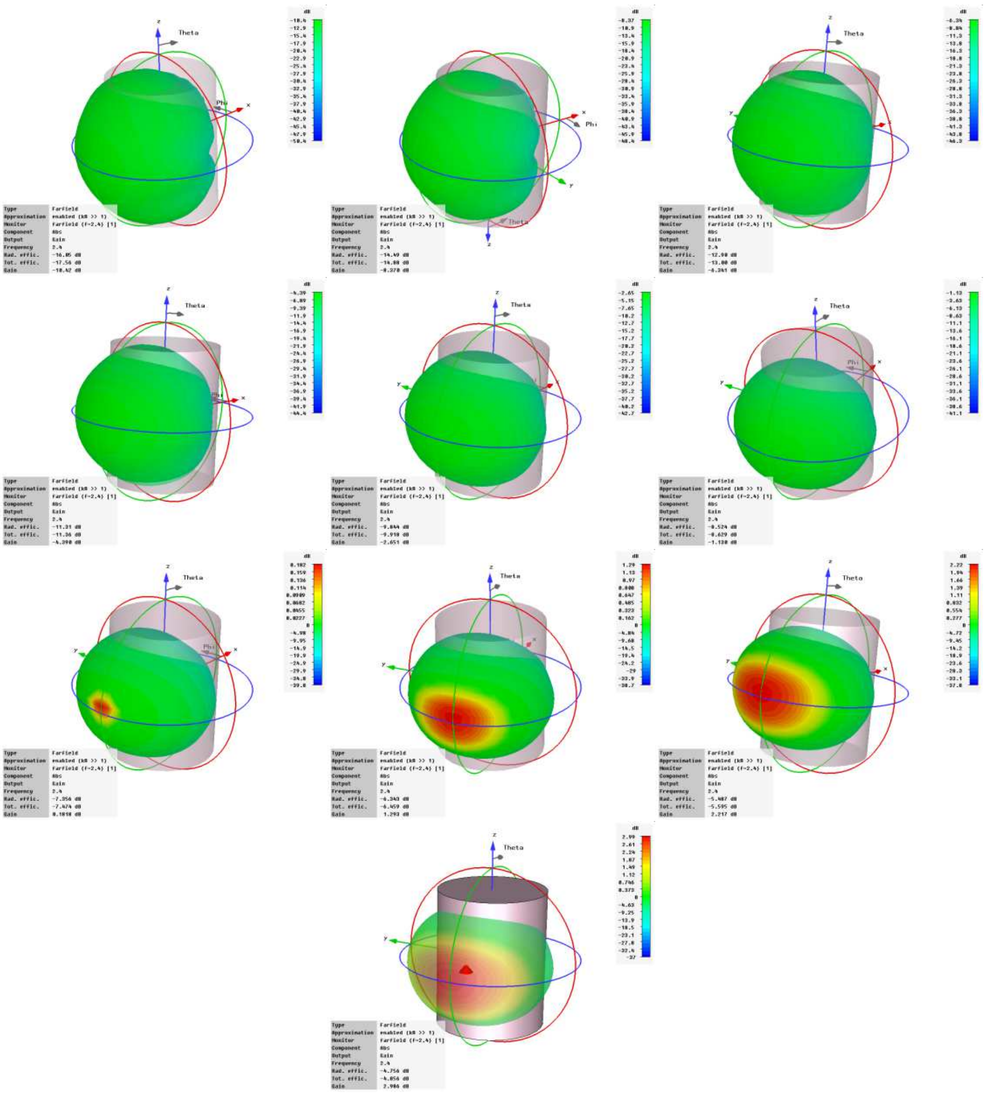

Figure 6-12 Gain pattern of half-wavelength dipole in the presence of the human body: distance from 1 to 10 mm

In Figure 6-13 we show the spherical wave decomposition of the dipole at 1mm from the phantom, using Jensen's normalization [Jen70]. We can clearly remark that higher modes appear because of the body perturbation. In Figure 6-14 we show an analysis by spherical wave expansion of the dipole close to the body at different distances. Each bar represents the normalized mode's power for each distance from the body. It can be seen that the powers mode distribution depends on the antenna-body separation and generally increase with the distance, because of the higher efficiency.

The analysis here presented, will be extended to other cases, with different antenna-body configurations, in order to realize an antenna model based on the distribution of spherical modes.

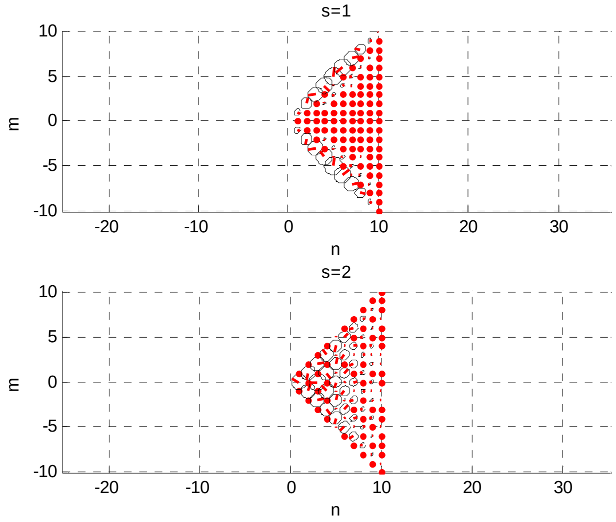

Figure 6-13 Spherical wave decomposition of the dipole at 1 mm from the body

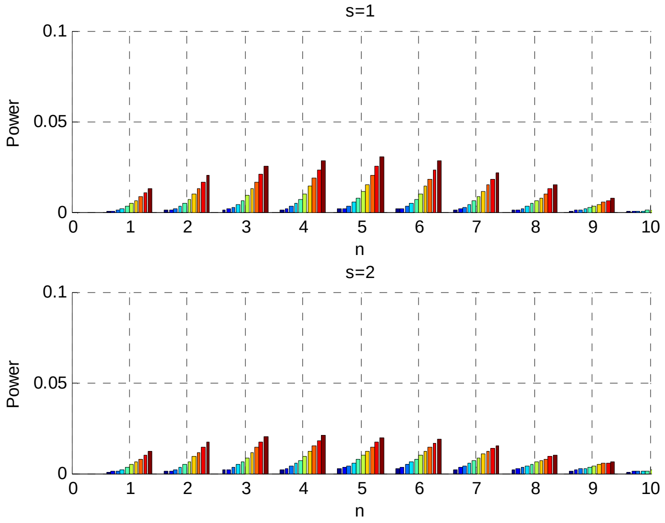

Figure 6-14 Power modes' distribution: bars corresponding to different distances with respect to the body

7. CONCLUSIONS

This deliverable has presented first important steps in the direction of elaborating a model that could represent efficiently the effect of the body on the antenna radiation pattern. A specific measurement campaign has been performed and exploited in order to derive such a representation. The proposed original model is based on a sparse decomposition of the antenna pattern on spherical harmonics. Two kinds of spherical harmonics decompositions have been presented and fully implemented. The careful analysis of one particular series (Series 2) has enabled to propose a simple model predicting the variation of an antenna pattern as a function of the antenna/phantom distance. However, this model has not been completely finalized yet. Indeed the relation between the geometrical configuration and the phase of the coefficients still needs to be clarified. The first attempt to have a purely statistical description of the phase information appears defective because it is unable to maintain the directivity information. However, we've been currently working on an alternative approach based on the geometrical theory of diffraction in order to capture the main features of the observed pattern deformations. This geometrical model would be applied either in the coefficient domain or in the angular domain. At that stage, it is however still hard to predict which approach would be the best option. Regarding this highly specific issue, one upcoming deliverable regarding physical simulations (i.e. D2.5) should provide firmer results and more details about the finally retained strategy.

As a side remark, note that the near field chamber used for this study was out of order during several months and that calibration/metrology problems (subsequent to other measurements not related to CORMORAN) have been harmful to the practical exploitation of some measurement data.

In addition to the measurement results, different antennas have been designed and simulated in the presence of the body in order to realize a database of antennas to be exploited for further models in T2.3 and T2.4. This database can be easily extended to take into account the variability of the on-body antenna performance, according to its topology and position, as well as to the phantom characteristics.

Overall, the work presented in this document is going to play a key role in the ongoing CORMORAN channel model definition and simulations. Generally speaking, the compact description of radiation patterns could be used to emulate the 3 kinds of links encountered in the CORMORAN scenarios (i.e. body-to-body, off-body and on-body).

For instance, for the situation of body-to-body and off-body links, the proposed antenna description will be directly incorporated in a deterministic ray tracing tool, avoiding a too complex search for the rays interacting with the body. The advantage here is to produce modified radiation patterns that directly include the effect of the presence of the body.

In this case, the body will be modeled as a set of articulated dielectric cylinders. The motion of those cylinders will be extracted from real motion capture files (e.g. C3D). Each antenna will have a unique invariant position with respect to local reference frame attached to each cylinder.

One key aspect of the proposed model is thus to provide a realistic time-varying test vector accounting for correlated and location-dependent links under agents' mobility in order to assist the design and evaluation of proper localization/communication algorithms based on those location-dependent radio parameters.

For each time step of a simulation based on such simple geometrical information, the radiation of the body-mounted antenna would then be instantiated properly with respect to relevant parameters such as the distance and orientation with respect to the cylinders. The proposed compact representation approach is as suitable for UWB as for narrow band systems. It could also be easily fed and/or complemented by simulations coming from simulation tools like CST.

In future works the preliminary antenna model presented here will be completed in order to be used in a full physical simulator for off-body and body-to-body communications. Actually antenna simulations, measurements and models will be combined with ray-tracing model, as an alternative to statistical modeling. In order to characterize the angular behavior of the off-body channel, other specific measurements with a realistic phantom have also been planned in parallel (See deliverable D2.2 and D2.3). These models will complete the statistical ones already presented in D2.2 and will realize the core of the 1st mobility-enabled PHY simulator expected in T2.5 (D2.5).

8. REFERENCES

[Swarztrauber1993] P.N. Swarztrauber "The vector harmonic transform method for solving partial differential equations in spherical geometry," Mon. Weather Review, AMS, 1993, 121, pp. 3415–3437.

[Roblin2008] C. Roblin, A. Sibille, "Ultra compressed parametric modeling of UWB antenna measurements using symmetries," 29th URSI General Assembly, Chicago, USA, August 2008, pp. 10–16

[Burghele2009] R. Burghelea, S. Avrillon and B. Uguen "Vector Spherical Harmonics Antenna Description for IR-UWB Ray Tracing Simulator," in Proc. ICEAA, 2009

[Burghelea2012] R. Burghelea, S. Avrillon, B. Uguen " Ultra-compact parametric modelling of three-dimensional antenna radiation pattern for impulse radio-ultra-wide band ray tracing", IET Microwaves, Antennas & Propagation, 2012, Vol 6, Is. 11, pp. 1251-1258

[Rahola2009] J. Rahola, F. Belloni, and A. Richter "Modelling of radiation patterns using scalar spherical harmonics with vector coefficients," in Proc. European Conference on Antennas and Propagation, 2009.

[Schmitz2102] A. Schmitz, T. Karolski, L. Kobbelt, "Using Spherical harmonics for Modeling Antenna Patterns", in Proc. Radio and wireless Symposium, 2012

[Wiesbeck2007] W. Wiesbeck, C. Sturm, W. Soergel, M. Porebska, G. Adamiuk, "Influence of antenna performance and propagation channel on pulsed UWB signals," in Proc. Int. Conf.

on Electromagnetics in Advanced Applications (ICEAA), Turin, Italy, 17– 21 September 2007, pp. 915–922

[Mac Namara] D.A. McNamara, C.W.I. Pistorius, J.A.G. Malherbe "Introduction the Uniform Geometrical Theory of Diffraction," Artech House, Boston

[SAM_standards] IEEE 1528; IEC 62209-1/IEC 62209-2; EN 50361:2001; EN 50383

[Thom] E. Gueguen, F. Thudor, P. Chambelin "A low cost UWB Printed Dipole Antenna with High Performances," in Proc. of the 2005 IEEE International Conference on Ultra-Wideband, Zurich, Sept. 5-8, 2005.

[Jen70] F. Jensen, "Electromagnetic near-field far-field correlations," Ph.D. dissertation LD 15, Lab. of Electromagnetic Theory, Technical University of Denmark, 1970.

9. ACKNOWLEDGEMENTS

The authors are grateful to Jerome Sol, who helped solving out some technical difficulties during the measurement campaign at UR1 premises, as well as to Laurent Crosnier and Christophe Guitton, who built the measurement platform in a very short period of time. Thank you for that.
The authors would also like to warmly thank Troels Pedersen, from Aalborg University, Denmark, for his highly active and valuable contributions to this work.